CrossMark

The Curious Case of ASASSN-20hx: A Slowly Evolving, UV- and X-Ray-Luminous, Ambiguous Nuclear Transient

Jason T. Hinkle[1] , Thomas W.-S. Holoien[2,16] , Benjamin. J. Shappee[1] , Jack M. M. Neustadt[3] , Katie Auchettl[4,5,6] ,
Patrick J. Vallely[3], Melissa Shahbandeh[7] , Matthias Kluge[8,9] , Christopher S. Kochanek[3,10] , K. Z. Stanek[3,10],
Mark E. Huber[1] , Richard S. Post[11], David Bersier[12] , Christopher Ashall[1] , Michael A. Tucker[1,17] , Jonathan P. Williams[1] ,
Thomas de Jaeger[1], Aaron Do[1], Michael Fausnaugh[13], Daniel Gruen[8,14] , Ulrich Hopp[8,9] , Justin Myles[15] ,
Christian Obermeier[8,9] , Anna V. Payne[1,18] , and Todd A. Thompson[3,10]
[1] Institute for Astronomy, University of Hawaiʻi, 2680 Woodlawn Drive, Honolulu, HI 96822, USA; jhinkle6@hawaii.edu
[2] The Observatories of the Carnegie Institution for Science, 813 Santa Barbara Street, Pasadena, CA 91101, USA
[3] Department of Astronomy, The Ohio State University, 140 West 18th Avenue, Columbus, OH 43210, USA
[4] School of Physics, The University of Melbourne, Parkville, VIC 3010, Australia
[5] ARC Centre of Excellence for All Sky Astrophysics in 3 Dimensions (ASTRO 3D), Australia
[6] Department of Astronomy and Astrophysics, University of California, Santa Cruz, CA 95064, USA
[7] Department of Physics, Florida State University, 77 Chieftan Way, Tallahassee, FL 32306, USA
[8] University-Observatory, Ludwig-Maximilians-University, Scheinerstrasse 1, D-81679 Munich, Germany
[9] Max Planck Institute for Extraterrestrial Physics, Giessenbachstrasse, D-85748 Garching, Germany
[10] Center for Cosmology and Astroparticle Physics, The Ohio State University, 191 W. Woodruff Avenue, Columbus, OH 43210, USA
[11] Post Observatory, Lexington, MA 02421, USA
[12] Astrophysics Research Institute, Liverpool John Moores University, 146 Brownlow Hill, Liverpool L3 5RF, UK
[13] Department of Physics and Kavli Institute for Astrophysics and Space Research, Massachusetts Institute of Technology, Cambridge, MA 02139, USA
[14] Kavli Institute for Particle Astrophysics & Cosmology, P.O. Box 2450, Stanford University, Stanford, CA 94305, USA
[15] Department of Physics, Stanford University, 382 Via Pueblo Mall, Stanford, CA 94305, USA

Abstract

We present observations of ASASSN-20hx, a nearby ambiguous nuclear transient (ANT) discovered in NGC 6297 by the All-Sky Automated Survey for Supernovae (ASAS-SN). We observed ASASSN-20hx from -30 to 275 days relative to the peak UV/optical emission using high-cadence, multiwavelength spectroscopy and photometry. From Transiting Exoplanet Survey Satellite data, we determine that the ANT began to brighten on 2020 June 22.8 with a linear rise in flux for at least the first week. ASASSN-20hx peaked in the UV/optical 30 days later on 2020 July 22.8 (MJD = 59052.8) at a bolometric luminosity of $L = (3.15 \pm 0.04) \times 10^{43}$ erg s^{-1}. The subsequent decline is slower than any TDE observed to date and consistent with many other ANTs. Compared to an archival X-ray detection, the X-ray luminosity of ASASSN-20hx increased by an order of magnitude to $L_x \sim 1.5 \times 10^{42}$ erg s^{-1} and then slowly declined over time. The X-ray emission is well fit by a power law with a photon index of $\Gamma \sim 2.3$–2.6. Both the optical and near-infrared spectra of ASASSN-20hx lack emission lines, unusual for any known class of nuclear transient. While ASASSN-20hx has some characteristics seen in both tidal disruption events and active galactic nuclei, it cannot be definitively classified with current data.

Unified Astronomy Thesaurus concepts: Accretion (14); Active galactic nuclei (16); Black hole physics (159); Supermassive black holes (1663); Tidal disruption (1696)

Supporting material: data behind figure, machine-readable tables

1. Introduction

All massive galaxies are known to host supermassive black holes (SMBHs) in their centers (e.g., Magorrian et al. 1998; Kormendy & Ho 2013). These SMBHs play a critical role in moderating galaxy evolution through radiative and mechanical feedback (e.g., Kormendy & Ho 2013). Direct detections of inactive SMBHs are limited to our own SMBH (e.g., Ghez et al. 2005) or massive SMBHs in nearby galaxies due to the need to resolve the SMBHs' small sphere of influence (e.g.,

Ford et al. 1994; Atkinson et al. 2005; Gebhardt et al. 2011). Nonetheless, $\sim$1%–5% of galaxies in the local universe host actively accreting SMBHs (Haggard et al. 2010; Lacerda et al. 2020), easily identified as active galactic nuclei (AGNs; Kauffmann et al. 2003).

While the steady-state properties of AGNs provide the opportunity for detailed study across the electromagnetic spectrum (e.g., Sanders et al. 1988; Boroson & Green 1992; Reynolds 1997), AGNs are also known to vary in a stochastic manner. This includes both photometric (e.g., MacLeod et al. 2012) and spectroscopic (e.g., Bianchi et al. 2005) variability. Perhaps the most striking examples of AGN variability are the so-called changing-look AGNs (e.g., Denney et al. 2014; Shappee et al. 2014; MacLeod et al. 2016; Yang et al. 2018) characterized by the appearance or disappearance of broad emission lines over time. In addition to long-timescale changes in activity over several years, AGNs also undergo dramatic flaring behavior (e.g., Drake et al. 2009; Graham et al. 2017;

Trakhtenbrot et al. 2019a; Frederick et al. 2020) on much shorter timescales. In addition to flares occurring in unambiguous AGNs, there is a growing class of rapid turn-on events (e.g., Gezari et al. 2017; Trakhtenbrot et al. 2019b; Frederick et al. 2019; Gromadzki et al. 2019; Neustadt et al. 2020), characterized by the rapid appearance of a blue continuum and strong emission lines in galaxies that do not host obvious AGNs.

Beyond AGN activity, the tidal disruption of a star and the subsequent return of debris to the SMBH results in a luminous accretion flare (Rees 1988; Evans & Kochanek 1989; Phinney 1989; Ulmer 1999). These tidal disruption events (TDEs) can occur in any galaxy and are thus good probes of otherwise inactive SMBHs. While early theoretical work predicted that the TDE spectral energy distribution (SED) should peak in the soft X-ray band (e.g., Lacy et al. 1982; Rees 1988; Evans & Kochanek 1989; Phinney 1989), observational studies have discovered that TDE properties are quite varied (e.g., van Velzen et al. 2011; Holoien et al. 2014, 2016a; Hinkle et al. 2020a; Alexander et al. 2020; van Velzen et al. 2021). This includes a broad diversity in spectroscopic properties (Holoien et al. 2019a; Leloudas et al. 2019; Hung et al. 2020; van Velzen et al. 2021), the existence or lack of radio emission (Alexander et al. 2020), and the presence or lack of X-ray emission (Holoien et al. 2016a; Auchettl et al. 2017; Wevers 2020).

Optically selected TDEs show luminous UV/optical emission, which is well fit by a blackbody with a temperature on the order of 20,000–50,000 K (e.g., Gezari et al. 2012; Holoien et al. 2014, 2016a). TDE blackbody temperatures are often roughly constant throughout their evolution, although some objects experience temperature evolution (Holoien et al. 2019b; Hinkle et al. 2020a; van Velzen et al. 2021). This is in contrast to the UV/optical continuum emission from AGNs, which is well fit by a power law (e.g., Vanden Berk et al. 2001). Some TDEs also have soft X-ray emission (e.g., Holoien et al. 2016a, 2016b; Wevers et al. 2019a; Hinkle et al. 2021b), which can generally be described by a blackbody with kT $\sim$30–60 eV (Auchettl et al. 2017). Conversely, X-ray emission from AGNs is ubiquitous (e.g., Mushotzky et al. 1993) and harder than typical TDE X-ray emission (e.g., Ricci et al. 2017; Auchettl et al. 2018). AGN X-ray spectra are consistent with Comptonization (e.g., Poutanen & Svensson 1996) and often exhibit hard X-rays above $\sim$10 keV, far more energetic than X-rays usually seen for TDEs.

The photometric evolutions of TDEs and AGN-related flares also show drastic differences. The light curves of TDEs often exhibit a smooth and monotonic decline (e.g., Holoien et al. 2014, 2019b, 2020; Nicholl et al. 2020; Hinkle et al. 2021b; van Velzen et al. 2021). In particular, the high-cadence Transiting Exoplanet Survey Satellite (TESS; Ricker et al. 2015) light curve of the TDE ASASSN-19bt (Holoien et al. 2019a) illustrates the smoothness of TDE light curves. This is in stark contrast to the stochastic variability superimposed on some AGN flares (e.g., Frederick et al. 2019, 2020; Neustadt et al. 2020) and the existence of AGN flares with rebrightening episodes (e.g., Frederick et al. 2020; Malyali et al. 2021). In addition, the masses of SMBHs hosting TDEs occurring are relatively low ($M \lesssim 10^{7.5} M_\odot$ Wevers et al. 2017; van Velzen 2018) because the tidal radius for a main-sequence star around a higher-mass SMBH lies within the event horizon (e.g., Rees 1988).

The spectra of TDEs and AGN flares are also quite distinct. Optical TDE spectra are blue, often with very broad ($\gtrsim$10,000 km s^{-1}) H or He lines (e.g., Arcavi et al. 2014; Holoien et al. 2016a, 2016b; van Velzen et al. 2021). Some TDEs also exhibit emission from metal lines (e.g., Blagorodnova et al. 2017; Leloudas et al. 2019) or Bowen fluorescence features (e.g., Blagorodnova et al. 2017; Leloudas et al. 2019; van Velzen et al. 2021). These are in contrast to the typical spectra of AGN, which have emission from Balmer lines and forbidden lines such as [O III] and [N II]. The line widths seen in AGN spectra during outburst are relatively narrow, on the order of $\sim$2000 km s^{-1} (Frederick et al. 2020). Additionally, the UV spectra of TDEs and AGNs are distinct due to differences in the environments in which they occur. AGNs exhibit strong [Mg II] emission in the UV (Vanden Berk et al. 2001; Batra & Baldwin 2014), which is conspicuously absent in all TDE UV spectra (Brown et al. 2018; Hung et al. 2021). Interestingly, the line evolutions of TDEs and AGNs is also quite different. In most TDEs, there is a positive correlation between line luminosity and line width (e.g., Holoien et al. 2016a, 2019b; Hinkle et al. 2021b). AGNs show the opposite behavior, with emission-line widths increasing as the luminosity decreases (e.g., Peterson et al. 2004; Denney et al. 2009).

Despite their many differences, AGNs and TDEs both provide a detailed look at accretion physics (e.g., Merloni et al. 2003; Lodato & Rossi 2011; Guillochon & Ramirez-Ruiz 2015), and insight into the environment and growth of SMBHs (e.g., Antonucci 1993; Auchettl et al. 2018). Additionally, the observed emission from both TDEs and AGNs is sensitive to SMBH parameters like spin and mass (e.g., Reynolds 2014; Gafton & Rosswog 2019; Mockler et al. 2019; Reynolds 2019). Because of the low fraction of AGNs in local galaxies, comprehensive studies of both AGNs and TDEs are needed to provide a complete picture of such properties of SMBHs and galactic nuclei.

Fortunately, with the advent of transient surveys like the All-Sky Automated Survey for Supernovae (ASAS-SN; Shappee et al. 2014; Kochanek et al. 2017), the Asteroid Terrestrial Impact Last Alert System (Tonry et al. 2018), the Zwicky Transient Facility (ZTF; Bellm et al. 2019), and the Panoramic Survey Telescope and Rapid Response System (Chambers et al. 2016), many more TDEs and AGN flares are being discovered. In addition, ground-based surveys have begun to discover an increasing number of ambiguous nuclear transients (ANTs), which cannot be neatly classified into either source class. Examples of such objects include ASASSN-18jd (Neustadt et al. 2020), ASASSN-18el (Trakhtenbrot et al. 2019a; Ricci et al. 2020), and the ANT studied here, ASASSN-20hx. These sources represent a unique opportunity to probe the variety of SMBH triggering mechanisms and search for broad trends among SMBH accretion behaviors.

In this paper, we present the discovery and observations of ASASSN-20hx. This paper is organized as follows. In Section 2, we detail the discovery and observations of the ANT. In Section 3, we present our analysis. Section 4 provides a discussion of our results, and finally, we summarize our findings in Section 5. Throughout the paper, we assume a cosmology of $H_0 = 69.6$ km s^{-1} Mpc^{-1}, $\Omega_M = 0.29$, and $\Omega_\Lambda = 0.71$.

2. Discovery and Observations

ASASSN-20hx ($\alpha, \delta = $ 17:03:36.49, +62:01:32.34) was discovered in the g-band data from the ASAS-SN "Brutus" unit on Haleakalā Hawai'i on 2020 July 10.3 UTC (Brimacombe et al. 2020). Its discovery was announced on the Transient Name Server, and assigned the name AT 2020ohl.[19] Rather than anonymize the discovering survey, we will continue to refer to the ANT by its public survey name ASASSN-20hx. ASASSN-20hx is located in the nucleus of the elliptical galaxy NGC 6297, a nearby S0 galaxy (de Vaucouleurs et al. 1991) at a redshift of z = 0.01671 (Adelman-McCarthy et al. 2006), corresponding to a luminosity distance of 72.9 Mpc. Saulder et al. (2016) find a distance to NGC 6297 of 55.6 Mpc using fundamental plane relationships, but due to the large scatter in the fundamental plane, we will continue to use a distance of 72.9 Mpc throughout the remainder of this work.

Shortly after discovery, we obtained several spectroscopic observations. Spectra from both the SPectrograph for the Rapid Acquisition of Transients (SPRAT; Piascik et al. 2014) on the 2 m Liverpool Telescope (Steele et al. 2004) and the Low-Resolution Imaging Spectrometer (LRIS; Oke et al. 1995) on the 10 m Keck I telescope, showed a blue continuum with few strong spectral features compared to the Sloan Digital Sky Survey (SDSS; York et al. 2000) host spectrum (see Section 2.1). The strong blue continuum and a position consistent with the nucleus of the host galaxy made ASASSN-20hx a potential TDE candidate. Based on this, we triggered spectroscopic and ground-based photometric follow-up of ASASSN-20hx.

From these spectra and several Neil Gehrels Swift Gamma-Ray Burst Mission (Swift; Gehrels et al. 2004) observations, Hinkle et al. (2020b) classified the source as a TDE based on the observations of multiple blue spectra, a hot blackbody temperature, position in the center of the host galaxy, and the lack of spectral features usually associated with AGNs or supernovae (SNe). However, the X-ray emission from ASASSN-20hx is harder than a typical TDE (Lin 2020), and the subsequent evolution of ASASSN-20hx was unlike any known TDE, suggesting it is a more exotic transient.

2.1. Archival Data of NGC 6297

NGC 6297 has been observed by several surveys across the electromagnetic spectrum. We obtained ugriz and JHK_S images from SDSS Data Release 15 (Aguado et al. 2019) and the Two Micron All-Sky Survey (2MASS; Skrutskie et al. 2006; 2MASS 2020), respectively. We measured aperture magnitudes using a 15″.0 aperture radius in order to capture all of the galaxy light, and used several stars in the field to calibrate the magnitudes. We also measured a 15″.0 aperture near-UV (NUV) magnitude from the Galaxy Evolution Explorer (GALEX; Martin et al. 2005) images using gPhoton (Million et al. 2016). Finally, we obtained archival W1, W2, W3, and W4 magnitudes from the Wide-field Infrared Survey Explorer (WISE; Wright et al. 2010) AllWISE catalog (Wright et al. 2019; Cutri et al. 2021), giving us coverage from ultraviolet through mid-infrared wavelengths.

In order to constrain the possibility of the host galaxy being an AGN, we analyzed a range of archival data for NGC 6297. From an archival Swift X-ray Telescope (XRT; Burrows et al. 2005)
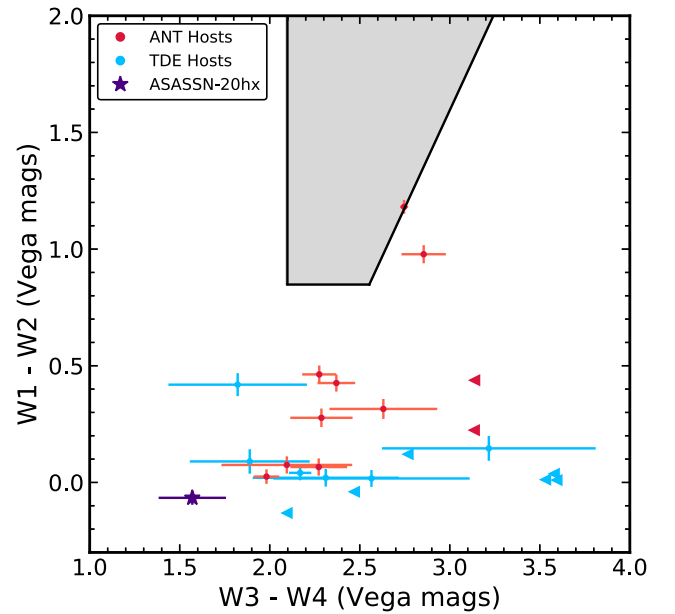
Figure 1. WISE color–color diagram used to discriminate strong AGNs from star-forming galaxies. The two colors used are $W1 - W2$ and $W3 - W4$ incorporating each of the WISE filters. The gray box is the AGN region determined by Assef et al. (2013). In addition to the host galaxy of ASASSN-20hx (purple point), we compare to other ANT hosts (red points) and TDE hosts (blue points) from the sample of Hinkle et al. (2021a). Like ASASSN-20hx, few of these hosts are selected as a strong AGN.

epoch taken ∼385 days prior to discovery, we find weak X-ray emission from the host galaxy at a level of 0.012 ± 0.007 counts s^{-1}. Assuming an AGN with a photon index of $\Gamma = 1.75$ (e.g., Ricci et al. 2017) and a Galactic column density of $N_H = 2.0 \times 10^{20}$ cm^{-2} along the line of sight (HI4PI Collaboration et al. 2016), this corresponds to an unabsorbed flux of $(5.0 \pm 3.0) \times 10^{-13}$ erg cm^{-2} s^{-1} in the 0.3–10 keV band. At the distance of NGC 6297, this yields an X-ray luminosity of $(3.4 \pm 2.1) \times 10^{41}$ erg s^{-1}. A detection at this level rules out strong AGN activity, and is consistent with a weak- or low-luminosity AGN (LLAGN; Tozzi et al. 2006; Marchesi et al. 2016; Liu et al. 2017; Ricci et al. 2017). We also measured UVW1 and U magnitudes from archival Swift images taken as part of the Swift Gravitational Wave Galaxy Survey (SGWGS; Evans et al. 2012). We find that over the span of roughly a year NGC 6297 brightened from $U = 16.86 \pm 0.04$ mag and $UVW1 = 18.46 \pm 0.08$ mag on $MJD = 58326.4$ to $U = 16.71 \pm 0.04$ mag and $UVW1 = 18.06 \pm 0.08$ mag on $MJD = 58655.1$. As the increased NUV magnitudes are coincident with the weak X-ray detection, this adds additional support to the statement that NGC 6297 may be a LLAGN.

The MIR colors of the host, $(W1 - W2) = -0.07 \pm 0.03$ mag and $(W3 - W4) = 1.57 \pm 0.19$ mag, also suggest that NGC 6297 does not harbor an AGN as luminous as the host galaxy (e.g., Assef et al. 2013). As shown in Figure 1, the host galaxy of ASASSN-20hx lies far from the AGN region and is bluer than most TDE and ANT hosts, consistent with light predominantly from stars. The NeoWISE mission (Mainzer et al. 2011; NEOWISE 2020) W1- and W2-band light curves show weak evidence for variability as the reduced χ^2 values for fitting them as a constant are 2.6 and 2.3, respectively.

We fit stellar population synthesis models to the archival photometry of NGC 6297 (shown in Table 1) using the Fitting

Table 1
Archival Host-galaxy Photometry

Filter	AB Magnitude	Magnitude Uncertainty
NUV	19.01	0.05
u	16.03	0.06
g	14.28	0.02
r	13.55	0.02
i	13.20	0.02
z	12.90	0.02
J	12.61	0.02
H	12.40	0.03
K_S	12.59	0.03
W1	13.65	0.02
W2	14.35	0.02

Note. Archival magnitudes of the host galaxy NGC 6297 used for our SED modeling. NUV, ugriz, and JHK_S magnitudes are 15″.0 aperture magnitudes measured from GALEX, SDSS, and 2MASS images, respectively. The W1 and W2 magnitudes are taken from the WISE AllWISE catalog. All magnitudes are presented in the AB system.

Table 2
Synthetic Host-galaxy Magnitudes

Filter	AB Mag	Mag Unc.	Observed Mag	Mag Unc.
UVW2	19.94	0.19	…	…
UVM2	19.69	0.13	…	…
UVW1	18.69	0.10	18.31	0.06
u	16.57	0.06	16.71	0.08
U	16.68	0.06	16.79	0.03
B	15.32	0.04	…	…
g	15.01	0.03	14.95	0.03
V	14.49	0.02	…	…
r	14.19	0.02	14.25	0.02
i	13.87	0.02	13.94	0.02
z	13.55	0.02	13.54	0.02
J	13.22	0.02	13.25	0.02
H	12.98	0.02	13.02	0.02

Note. Synthetic host magnitudes of NGC 6297 from our FAST SED fits to the 5″.0 magnitudes. These are used to subtract the fluxes of our follow-up photometry for which archival magnitudes are unavailable. The right columns indicated the observed archival magnitudes and their uncertainties. The archival Swift UVW1 and U magnitudes come from stacking the two SGWGS epochs. All magnitudes are presented in the AB system.

and Assessment of Synthetic Templates (FAST; Kriek et al. 2009) to obtain an SED of the host. Our fit assumes a Cardelli et al. (1988) extinction law with $R_V = 3.1$, Galactic extinction of $A_V = 0.064$ mag (Schlafly & Finkbeiner 2011), a Salpeter initial mass function (Salpeter 1955), an exponentially declining star formation rate, and the Bruzual & Charlot (2003) stellar population models. Based on the FAST fit, NGC 6297 has a stellar mass of $M_* = (4.2^{+0.5}_{-0.4}) \times 10^{10} M_\odot$, an age of $(4.7^{+0.7}_{-0.5})$ Gyr, and star formation rate of SFR $(2.3^{+0.9}_{-0.2}) \times 10^{-2} M_\odot$ yr^{-1}. Using the sample of Mendel et al. (2014) to compute a scaling relation between stellar mass and bulge mass, we estimate a bulge mass of $\sim 10^{10.5} M_\odot$. We then use the M_B–M_{BH} relation of McConnell & Ma (2013) to estimate a black hole mass of $\sim 10^{7.9} M_\odot$. This SMBH mass is higher than for most TDEs (Kochanek 2016; van Velzen 2018; Ryu et al. 2020).

Our photometric follow-up campaign includes several filters for which archival imaging data are not available, including the majority of the Swift UltraViolet and Optical Telescope (UVOT) and BVRI filters. In comparing our Swift and ground-based BV photometry, we found a better agreement when using the default Swift 5″.0 aperture radius rather than the larger 15″.0 radius. We therefore remeasured 5″.0 aperture magnitudes of the host galaxy in the NUV, ugriz, and JHK filters. We again fit stellar population synthesis models to this data using FAST. While this does not incorporate light from the entire host galaxy, we nevertheless find good agreement between the SFRs and ages estimated from the 15″.0 and 5″.0 fits. In order to estimate the host flux in these filters for host subtraction, we convolved the host SED from FAST with the filter response curve for each filter to obtain 5″.0 fluxes. To estimate uncertainties on the estimated host-galaxy fluxes, we perturbed the archival host fluxes assuming Gaussian errors and ran 1000 different FAST iterations. We present these 5″.0 synthetic magnitudes in Table 2. These synthetic fluxes were then used to subtract the host flux in our nonsurvey follow-up data.

We also examined the archival SDSS (York et al. 2000) spectrum of NGC 6297. This spectrum shows [N II] λ6584 and weak [O III] λλ4959, 5007 and [S II] λλ6717, 6731 emission with Balmer lines in absorption. Figure 2 shows the properties of NGC 6297 in several strong emission-line diagnostic

diagrams using the line fluxes from the Max Planck Institute for Astrophysics-Johns Hopkins University (MPA-JHU) catalog (Brinchmann et al. 2004). The left panel of Figure 2 compares the Hα emission-line equivalent width to the Lick Hδ$_A$ absorption index, which compares current and past star formation to identify post-starburst galaxies (e.g., French et al. 2016). The right panel of Figure 2 shows Hα emission equivalent width as compared to $\log_{10}([N\ II]/H\alpha)$ to separate ionization mechanisms, particularly those associated with LINER-like (low-ionization nuclear emission-line region) emission-line ratios. The background points show the general distribution of galaxies in the MPA-JHU catalog (Brinchmann et al. 2004) for SDSS DR8 (Eisenstein et al. 2011).

From Figure 2, we see that NGC 6297 lies in the large cloud of points corresponding to galaxies without active star formation, consistent with the SED modeling. In fact, the Lick Hδ$_A$ absorption index is lower than most of the TDE host galaxies. The WHAN (Hα equivalent width versus [N II]/Hα) diagram of Figure 2 places NGC 6297 near the *retired galaxies* (RG) region, where galaxies have ceased actively forming stars and are predominantly ionized by hot low-mass evolved stars such as post-AGB stars (Cid Fernandes et al. 2011). However, the host lies slightly outside the cloud of RG points and toward the passive galaxies region, supported by the lack of current star formation in the galaxy.

While the SDSS spectrum shows only weak emission lines, affecting typical BPT analysis (Baldwin et al. 1981), we include the commonly studied emission-line ratio measurements here for completeness. The line ratios $\log_{10}([O\ III]/H\beta) = 0.33 \pm 0.13$, $\log_{10}([N\ II]/H\alpha) = -0.07 \pm 0.08$, and $\log_{10}([S\ II]/H\alpha) = -0.44 \pm 0.21$ place this galaxy in the AGN region of the [N II]/Hα diagram and the H II region of the [S II]/Hα diagram (Baldwin et al. 1981; Veilleux & Osterbrock 1987). Given this disagreement and the large uncertainties, the dominant ionization mechanism is uncertain in this galaxy. Combinations of star formation, AGN activity, and shocks are known to produce intermediate line ratios such as those seen for NGC 6297 (e.g., Davies et al. 2014; D'Agostino et al. 2019). We note that the
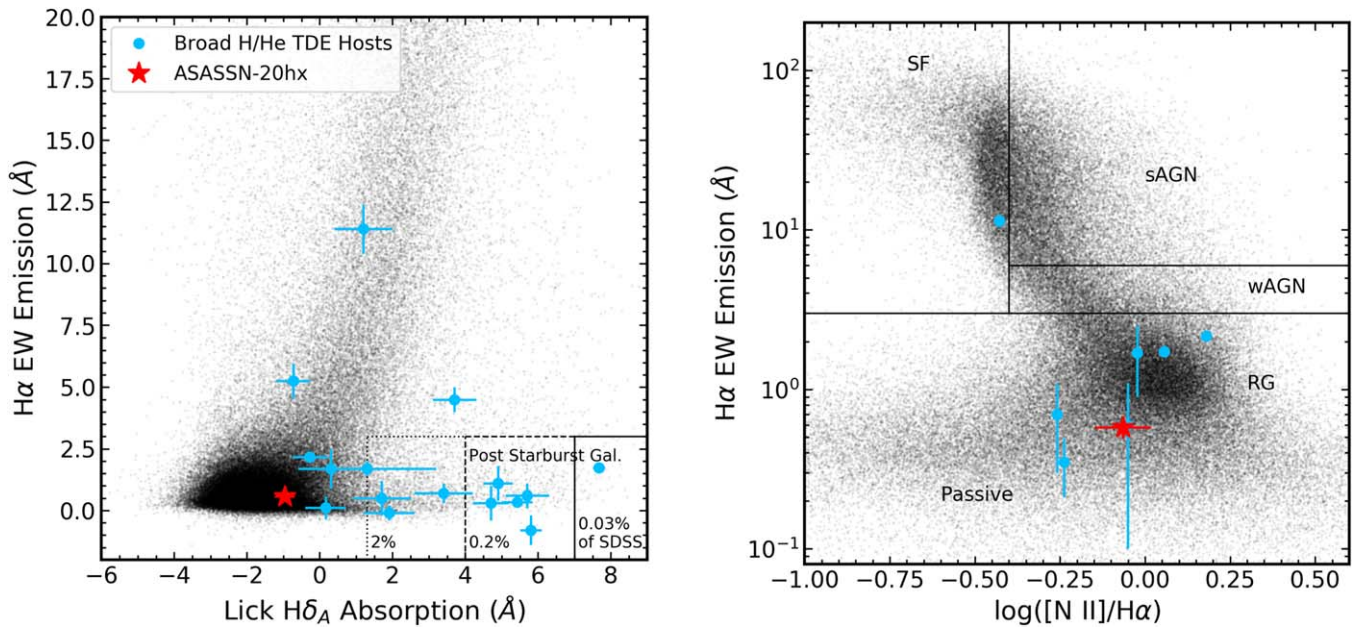
Figure 2. Left panel: Hα emission-line equivalent width (EW), which traces current star formation, as compared to the Lick Hδ_A absorption index, which traces star formation in the past Gyr. The host galaxy NGC 6297 is shown as a red star, with TDE hosts shown as blue circles. NGC 6297 lies in the large cloud of points with little current or recent star formation. The error bars on NGC 6297 are roughly the size of the symbol. Right panel: Hα emission-line EW (W$_{H\alpha}$), as compared to log$_{10}$([N II]/Hα), otherwise known as the WHAN diagram (Cid Fernandes et al. 2011). Lines separating star-forming galaxies (SF), strong AGN (sAGN), weak AGN (wAGN), and passive and *retired galaxies* (RG) are shown (Cid Fernandes et al. 2011). In all panels, galaxies from SDSS Data Release 8 (Eisenstein et al. 2011) are shown in black.
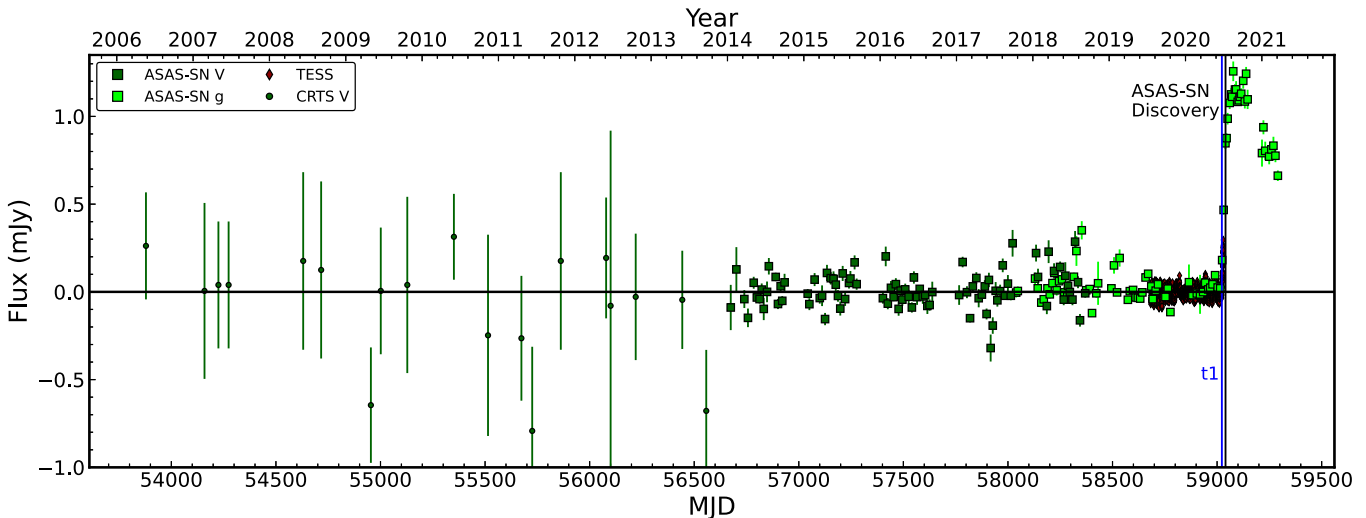
Figure 3. Long-term host-subtracted light curve of NGC 6297 from CRTS, ASAS-SN, and TESS. Dark green circles show CRTS *V*-band data stacked in 50 days bins. Squares represent ASAS-SN photometry, with dark green showing *V*-band data and light green showing *g*-band data. The ASAS-SN data is stacked in 10 days bins prior to the flare and 5 days bins after the flare. Red diamonds show TESS data in 2 hr bins. The horizontal black line represents zero flux. The vertical blue line is the time of first light obtained from our fit to the TESS data, and the vertical black line marks the time of the ASAS-SN discovery.

fraction of detected Seyferts and LINERs in S0 galaxies is ~12% and ~26%, respectively (Ho 2008). This strengthens the case that NGC 6297 may host a LLAGN.

In addition to our spectroscopic analysis of the host galaxy of ASASSN-20hx, we also looked for nuclear variability using archival Catalina Real-Time Transient Survey (CRTS; Drake et al. 2009), ASAS-SN, and TESS. CRTS uses SExtractor (Bertin & Arnouts 1996) photometry, which both includes flux from the host galaxy and makes the light curve noisy. We simply subtracted the mean flux as an estimate of the host contamination. These light curves are shown in Figure 3. No significant variability is seen over this timescale.

2.2. ASAS-SN Light Curve

ASAS-SN is a fully automated transient survey consisting of 20 individual telescopes on 5 robotic mounts. Each telescope is a 14 cm aperture Nikon telephoto lens with 8″.0 pixels, and each unit consists of 4 telescopes sharing a common mount. The five ASAS-SN units are located at Haleakalā Observatory, McDonald Observatory, the South African Astrophysical Observatory, and two at Cerro Tololo Inter-American Observatory. With this current telescope network, ASAS-SN monitors the visible sky with a cadence of ~20 hr to a depth of *g* ~ 18.5 mag.

The images were reduced using the automated ASAS-SN pipeline, which incorporates the ISIS image subtraction package (Alard & Lupton 1998a; Alard 2000). As we have several years of ASAS-SN *g*-band photometry prior to the ASASSN-20hx outburst, we built a reference image using good images from multiple cameras observed at least a month before the fit time of first light. This common reference image was then subtracted from all the *g*-band data. The ASAS-SN *V*-band data was reduced using the default ASAS-SN pipeline and references as there is no transient flux seen in any *V*-band epoch.

We then used the IRAF `apphot` package with a 2-pixel radius (approximately 16″.0) aperture to perform the aperture photometry on each subtracted image, generating a differential light curve. Our photometry was calibrated using the AAVSO Photometric All-Sky Survey (Henden et al. 2015). We discarded images with a FWHM of 1.67 pixels or greater. We stacked the pre-flare ASAS-SN data in 10 days bins to get deep early time limits.

2.3. TESS Observations

The host galaxy of ASASSN-20hx, NGC 6297, lies in the TESS northern continuous viewing zone near the North Ecliptic Pole, so it was observed continuously between 2019 July 18 and 2020 July 04. While the ASASSN-20hx flare was only observed in Sector 26 at the very end of Cycle 2, we nevertheless have almost a full year of high-precision photometry to search for prior variability and study the onset of the flare.

Similar to our ASAS-SN data reduction, we used the ISIS package (Alard & Lupton 1998a; Alard 2000) to perform image subtraction on the TESS full-frame images (FFIs) to produce light curves (see Vallely et al. 2019; Fausnaugh et al. 2021; Vallely et al. 2021). Because of TESS's large pixel scale, we constructed independent reference images for each sector. To do this, we selected the first 100 FFIs of good quality obtained in each sector, excluding images with sky background levels or point-spread function widths above average for the sector. We excluded all FFIs with data quality flags. We also used several conservative quality cuts such as excluding FFIs obtained when the spacecraft pointing was compromised, when TESS was affected by an instrument anomaly, or when significant background effects due to scattered light were present in the images.

We converted the measured fluxes into TESS-band magnitudes using an instrumental zero-point of 20.44 electrons per second in the FFIs, based on the TESS Instrument Handbook (Vanderspek et al. 2018). The single TESS filter spans roughly 6000–10000 Å with an effective wavelength of $\sim$7500 Å. We show the host-subtracted light curve for all TESS sectors in Figure 4. We also show TESS photometry stacked in 1 day bins using a weighted average to compare to our ground-based photometry. Other than the ASASSN-20hx flare, there are no significant outbursts above a flux of $\sim$0.1 mJy in the FFIs. This corresponds to an AB mag of 18.9, placing strong constraints on optical host variability in the year prior to ASASSN-20hx. Indeed if we conduct the same exercise with the stacked photometry, the limit is even more constraining at $\sim$0.06 mJy or an AB magnitude of 19.5. The root-mean-squared values are 44 and 36 μJy, respectively, for the FFIs and the stacked data. We can also use the stacked photometry to compute an approximate Eddington ratio. If we use the scatter of the
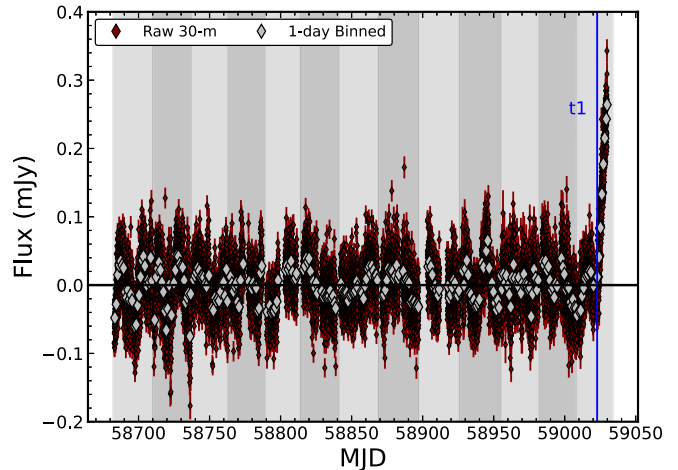

Figure 4. TESS light curve of NGC 6297. The red diamonds are raw 30 m FFI data, and the silver diamonds are TESS data stacked in 1 day bins. The alternating shading represents the various sectors for which TESS observed the source. The vertical blue line is the time of first light obtained from our fit to the TESS data.

stacked TESS photometry as a rough estimate of preexisting AGN variability, we find a luminosity limit in the TESS band of $\lesssim 6 \times 10^{40}$ erg s^{-1}. This corresponds to an Eddington ratio of $\lesssim 6 \times 10^{-6}$ using the SMBH mass computed from galaxy scaling relations. Although this is a rough estimate, using only a single photometric band, it is clear that the host galaxy of ASASSN-20hx was not previously a highly variable AGN.

2.4. Additional Ground-based Photometry

In addition to the ASAS-SN and TESS survey photometry, we obtained photometric follow-up observations from several ground-based observatories. We used the Las Cumbres Observatory Global Telescope (LCOGT) network (Brown et al. 2013) 1 m and 2 m telescopes located at Haleakalā and McDonald Observatory for *BVgri* observations, the Liverpool 2 m telescope at Observatorio del Roque de los Muchachos for *ugriz* observations, the Wendelstein Observatory 2 m Fraunhofer telescope for *ugizJH* observations, and images from amateur astronomer Richard Post (RP) for *BVgri* observations taken with a 24-in and 32-in telescope. After applying appropriate flat-field corrections, we obtained the astrometry for each image using astrometry.net (Barron et al. 2008; Lang et al. 2010).

For our ground-based data, we used `apphot` to measure 5″.0 aperture magnitudes of the host plus transient emission, and subtracted the 5″.0 host flux synthesised from our FAST fit in the appropriate filter to isolate the transient flux. Although there were archival SDSS images in the *ugriz* filters, we found that host subtraction yielded significant artifacts and scatter in the subtracted images and magnitudes. For each filter, we used SDSS stars in the field to calibrate our photometry, using the corrections from Lupton (2005) to calibrate the *B*- and *V*-band magnitudes with the *ugriz* data. We found an offset between the ground-based and ASAS-SN *g*-band data, which we corrected by shifting the median of ground-based *g* band to match the median ASAS-SN *g*-band mag.

We measured the centroid position of the transient in a host-subtracted LCOGT *g*-band image taken near the peak using the IRAF `imcentroid` package. This yielded a position of (α, δ) = (17:03:36.560, +62:01:32.18). We used the archival

SDSS g-band image to measure the position of the nucleus of NGC 6297, finding $(\alpha, \delta) = (17:03:36.555, +62:01:32.22)$. This gives an angular offset of $0''.094 \pm 0''.222$, where the uncertainty is due to uncertainty in the centroid positions of ASASSN-20hx and the host nucleus. As the transient position is consistent with the nucleus, we do not include the uncertainty due to the astrometric solution, which would only inflate the total error. At the host distance, this offset corresponds to a physical distance of 33.2 ± 78.4 pc.

2.5. Swift Observations

Sixty-two total Neil Gehrels Swift Gamma-Ray Burst Mission (Swift; Gehrels et al. 2004) target-of-opportunity observations were carried out between 2020 July 19 and 2021 April 15 (Swift target ID 13617, PIs: Holoien, Hinkle). Some of these epochs were obtained from Swift guest investigator program 1619122 (PI: Holoien). These observations used the UVOT (Roming et al. 2005) and the XRT (Burrows et al. 2005) to study the multiwavelength properties of the ANT.

2.5.1. UVOT Observations

For a majority of the observation epochs, Swift observed ASASSN-20hx with all six UVOT filters (Poole et al. 2008): V (5425.3 Å), B (4349.6 Å), U (3467.1 Å), UVW1 (2580.8 Å), $UVM2$ (2246.4 Å), and UVW2 (2054.6 Å). The wavelengths quoted here are the pivot wavelengths calculated by the SVO Filter Profile Service (Rodrigo et al. 2012). Each epoch of UVOT data includes 2 observations in each filter, which we combined into one image for each filter using the HEASoft `uvotimsum` package. We then used the `uvotsource` package to extract source counts using a $5''.0$ radius region centered on the position of the ANT and background counts using a source-free region with radius of $\sim110''.0$. We converted the UVOT count rates into fluxes and magnitudes using the most recent calibrations (Poole et al. 2008; Breeveld et al. 2010).

Because the UVOT uses unique B and V filters, we used publicly available color corrections[20] to convert the UVOT BV data to the Johnson-Cousins system. We then corrected the UVOT photometry for Galactic extinction and removed host contamination by subtracting the corresponding $5''.0$ host flux in each filter, as we did with the ground-based BV data.

Figure 5 shows the extinction-corrected, host-subtracted light curves of ASASSN-20hx. The photometry spans from the shortest UVW2 (2054.6 Å) band of Swift to z band (~8947 Å) from Liverpool Telescope (LT) and Wendelstein and includes data ranging from 30 days prior to the peak to 275 days after the peak. All the UV and optical photometry shown in Figure 5, and the limits not shown in this figure are presented in Table 3.

2.5.2. XRT Observations

ASASSN-20hx was also observed using the Swift-XRT in photon-counting mode. All observations were reduced using the standard filter and screening criteria specified in the Swift-XRT reduction guide[21] and the most up to date calibration files. Here, we reprocessed level-one XRT data using the task

XRTPIPELINE version 0.13.2, producing cleaned event files and exposure maps for all observations.

To extract background-subtracted count rates from each individual observation, we used a $20''.0$ source region centered on the position of ASASSN-20hx and a source-free background region with a radius of $150''.0$ centered at $(\alpha, \delta) = (17^h02^m36.19^s, +62°02'22''.64)$. All extracted count rates were corrected for the encircled energy fraction.[22]

To increase the S/N of our observations, we also combined our individual Swift-XRT observations using XSELECT version 2.4k. Here we combined the observations into 12 time bins spanning the ~300 day Swift observing campaign. This allowed us to extract spectra with ~500 background-subtracted counts using the task XRTPRODUCTS version 0.4.2 and the source and background regions defined above. Ancillary response files (ARF) were generated using the task XRTMKARF and the individual exposure maps that were generated by XRTPIPELINE and then merged using XIMAGE version 4.5.1. The response matrix files (RMFs) are ready-made files that we obtained from the most recent calibration database. Each spectrum was grouped to have a minimum of 15 counts per energy bin using the FTOOLS command GRPPHA.

2.6. NICER Observations

ASASSN-20hx was also observed using the X-ray timing instrument on board the Neutron star Interior Composition ExploreR (NICER: Gendreau et al. 2012), which is an external payload on the International Space Station. NICER offers high spectral (~85 eV at 1 keV) and time resolution (~100 ns) observations in the 0.2–12 keV energy range and has been used to observe a number of nuclear transients (Trakhtenbrot et al. 2019a; Pasham et al. 2020a, 2020b; Pasham & Gendreau 2020; Payne et al. 2022; Hinkle et al. 2021b; Wevers et al. 2021; Cannizzaro et al. 2021; Ricci et al. 2021). ASASSN-20hx was observed a total of 41 times between 2020 July 25 and 2020 November 01 (ObsIDs: 3573010101–3573014102, PI: Auchettl), for a total cumulative exposure of 67.6 ks.

The data were reprocessed using the NICERDAS version 7a and the task NICERL2. Here standard filtering criteria were used,[23] as well as the latest gain and calibrations files. Time-averaged spectra and count rates were extracted using XSELECT, while we took advantage of ready-made ARF (nixtiaveonaxis20170601v004.arf) and RMF (nixtiref20170601v002.rmf) files that are available with the NICER CALDB. All spectra was grouped using a minimum of 20 counts per energy bin. As NICER is a nonimaging instrument, background spectra were generated using the background modeling tool NIBACKGEN3C50.[24]

To analyze the spectral data from both Swift and NICER, we used the X-ray spectral fitting package (XSPEC) version 12.11.1 (Arnaud 1996) and χ^2 statistics. Both the Swift and NICER data and their analysis are further discussed in Section 3.5. Table 4 shows the X-ray luminosities and hardness ratios for the Swift XRT and NICER epochs analyzed in this work.

---

[20] https://heasarc.gsfc.nasa.gov/docs/heasarc/caldb/swift/docs/uvot/uvot_caldb_coltrans_02b.pdf
[21] http://swift.gsfc.nasa.gov/analysis/xrt_swguide_v1_2.pdf

[22] A $20''.0$ source radius contains $\sim80\%$ of the source counts at 1.5 keV, assuming an on-axis pointing (Moretti et al. 2004)
[23] See Bogdanov et al. (2019) or Section 2.7 of Hinkle et al. (2021a)
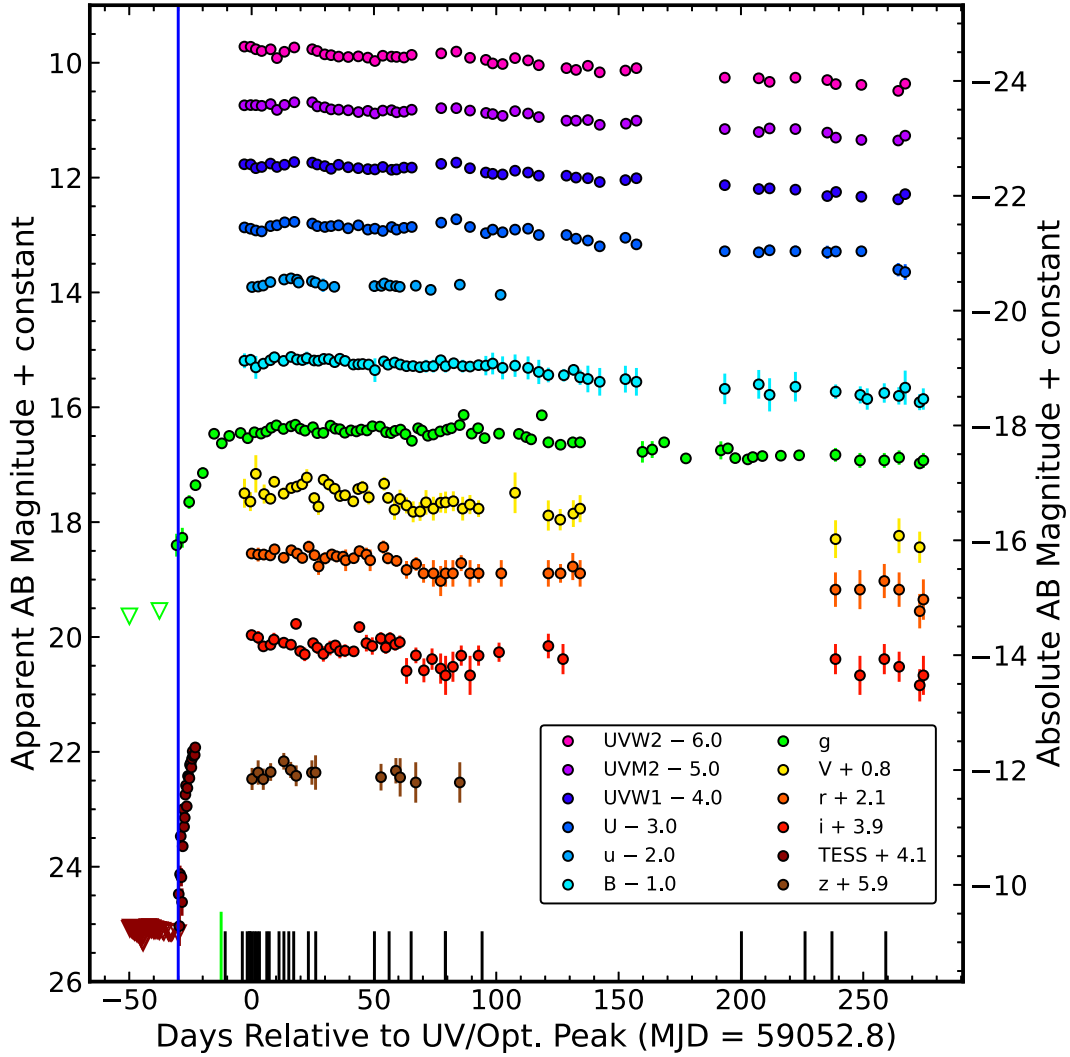[24] https://heasarc.gsfc.nasa.gov/docs/nicer/tools/nicer_bkg_est_tools.html

Figure 5. Host-subtracted UV and optical light curves of ASASSN-20hx, showing ASAS-SN (*g*), Swift (UV+*UBV*), Las Cumbres Observatory 1 m telescopes (*BVgri*), Liverpool Telescope (*ugriz*), RP (*BVgri*), and Wendelstein (*ugiz*) photometry stacked in 2 days bins. The TESS photometry is shown in 6 hr bins. The photometry spans from roughly 50 days prior to the peak (MJD = 59052.8) to roughly 275 days after in observer-frame days. Horizontal error bars on the data indicate the date range of observations stacked to obtain deeper limits and higher S/N detections, although they are often smaller than the symbols. Open symbols indicate 3σ upper limits and are only shown for the early time data. The green bar on the *x*-axis marks the epoch of ASAS-SN discovery. The black bars along the *x*-axis show epochs of spectroscopic follow-up. The blue line is the estimated time of first light (see Section 3.1) with uncertainty comparable to the line width. The time over which the first ASAS-SN detection is stacked is consistent with the time of first light. All data are corrected for Galactic extinction and shown in the AB system.

Table 3
Host-subtracted Photometry of ASASSN-20hx

MJD	dMJD$_{hi}$	dMJD$_{lo}$	Filter	Magnitude	Uncertainty
59049.85	0.75	0.71	UVW2	15.72	0.03
59052.41	0.65	1.06	UVW2	15.72	0.02
59054.52	0.00	0.00	UVW2	15.77	0.04
...	...	...	...	...	...
59126.00	0.00	0.00	z	15.98	...
59137.89	0.00	0.00	z	16.63	0.35
59149.00	0.00	0.00	z	16.26	...

Note. Host-subtracted magnitudes and 3σ upper limits for all follow-up photometry. The MJD errors correspond to the range over which data were stacked. All magnitudes are corrected for Galactic extinction and presented in the AB system. Only a small section of the table is displayed here to show the format. We do not show the *J*- and *H*-band data as they are mostly upper limits, and any detections are likely spurious. The full table can be found online as an ancillary file.

(This table is available in its entirety in machine-readable form.)

Table 4
X-Ray Luminosities and Hardness Ratios of ASASSN-20hx

MJD	log(L (erg s^{-1}))	*L* Error	HR	HR Error	Satellite
59049.14	42.32	0.04	−0.73	0.13	Swift
59050.60	42.30	0.04	−0.60	0.07	Swift
59051.35	42.06	0.05	−0.62	0.11	Swift
...	...	...	...	...	...
59317.09	41.74	0.10	−0.69	0.31	Swift
59319.93	41.60	0.15	−0.79	0.00	Swift
59346.30	41.96	0.05	−0.43	0.05	Swift

Note. X-ray luminosities and hardness ratios with associated uncertainties. The hardness ratio is defined as (H−S)/(H+S), where we define hard counts H as the number of counts in the 2–10 keV range and soft counts S are the number of counts in the 0.3–2 keV. The last column reports the source of the data for each epoch. Only a small section of the table is displayed here. The full table can be found online as an ancillary file.

(This table is available in its entirety in machine-readable form.)

2.7. Spectroscopic Observations

In addition to our classification spectra obtained from SPRAT and LRIS, we obtained follow-up spectra of ASASSN-20hx with the SuperNova Integral Field Spectrograph (SNIFS; Lantz et al. 2004) on the 88-inch University of Hawaii telescope (UH88), LRIS on the 10 m Keck I telescope, SPRAT on the 2 m Liverpool Telescope, and the Multi-Object Double Spectrographs (MODS; Pogge et al. 2010) on the Large Binocular Telescope (LBT; Hill et al. 2006). Three of our spectra were obtained prior to the peak light, and nineteen were obtained after the peak. Most of the spectra were reduced and calibrated with standard IRAF procedures, such as bias subtraction, flat-fielding, 1D spectroscopic extraction, and wavelength calibration. The LRIS spectra were reduced in part using LPipe (Perley 2019). The SNIFS spectra were calibrated using a custom reduction pipeline. The flux calibration for our observations was initially done using the standard star spectra obtained on the same nights as the science spectra and then refined using our follow-up photometry and blackbody fit results.

All the classification and follow-up optical spectra for ASASSN-20hx are presented in Figure 6. From top to bottom, the optical spectrum remains blue and largely featureless throughout the evolution. Nonetheless, the spectra do show some absorption lines of Hα, Hβ, Ca II H and K, and Na I D, although these are likely contamination from the bright host galaxy. The locations of several emission lines commonly seen in TDEs and AGNs are marked with vertical dashed lines. None of these lines appear in emission throughout the time period probed by these spectra.

In addition to our optical spectra, we obtain three near-infrared (NIR) spectra of ASASSN-20hx with SpeX (Rayner et al. 2003) on the NASA Infrared Telescope Facility (IRTF). These data were obtained in the short cross-dispersed mode giving us coverage over roughly the *zYJHK* bands at moderate resolution. These spectra were reduced and calibrated with standard IRAF procedures, such as bias subtraction, flat-fielding, 1D spectroscopic extraction, and wavelength calibration. When possible, a telluric standard from the same night was used to remove atmospheric contamination.

2.8. Submillimeter Observations

We obtained submillimeter observations in the 850 μm band (353 GHz) using the Submillimetre Common-User Bolometer Array 2 (SCUBA-2; Holland et al. 2013) on the James Clerk Maxwell Telescope (JCMT). As the expected emission from ASASSN-20hx would be a point source, we used a simple constant-velocity Daisy mapping pattern. These data were calibrated and reduced using the default SCUBA-2 pipeline at the Canadian Astronomical Data Centre[25] with phase and flux calibrators taken on the same night as the source observations. We discuss the derived submillimeter limits of ASASSN-20hx relative to the known TDEs in Section 3.2.

3. Analysis

Here we present the analysis of the UV/optical light curve, submillimeter limits, optical and NIR spectroscopy, the SED, and X-rays to place ASASSN-20hx in context with other transients. While the long plateau phase of the light curve is

reminiscent of Type IIP SN, the length of this phase is longer than even the most extreme of these SNe (e.g., Sanders et al. 2015; Reguitti et al. 2021). Additionally, the spectra are inconsistent with a SN II as they lack hydrogen features. The spectra are formally consistent with a Type Ic SN, but the strong, persistent X-ray emission and the long-lived light curve are not (e.g., Taddia et al. 2018). Additionally, ASASSN-20hx bears some similarities to the constant temperature and lack of strong emission lines in some luminous red novae (e.g., Blagorodnova et al. 2020). However, this scenario is not likely due to ASASSN-20hx being much hotter and several orders of magnitude more luminous. Because the observed properties of ASASSN-20hx are incompatible with known SNe and stellar transients, we focus the remainder of this manuscript on distinguishing between TDE and AGN activity.

3.1. Light Curve

Using Markov Chain Monte Carlo (MCMC) methods, we fit each of the epochs with Swift UV photometry as a blackbody to obtain the bolometric luminosity, temperature, and effective radius of ASASSN-20hx. To keep our fits relatively unconstrained, we ran each of our blackbody fits with flat temperature priors of 10,000 K $\leqslant$ T $\leqslant$ 55,000. We find that a blackbody model adequately describes the UV/optical emission, with a median reduced χ^2 of $\sim$1.3, similar to or better than previous TDE candidates (e.g., Holoien et al. 2014). To obtain the time of peak UV/optical luminosity, we fit a parabola to the light curve created by bolometrically correcting the ASAS-SN *g*-band light curve using these blackbody fits, excluding the upper limits. Because the curve is quite flat near the peak, we fit the parabola in a narrow range between MJD = 59029.9 and MJD = 59061.0. Despite the flatness of the light curve, we find a median reduced χ^2 of 1.4, indicating that the parabola is an acceptable fit. We generated 10,000 realizations of the bolometric light curve in this date range with each luminosity perturbed by its uncertainty assuming Gaussian errors. We then fit a parabola to each perturbed light curve and took the median value as the peak and 16th and 84th percentiles as the uncertainties in peak time. Using this procedure, we find the time of peak bolometric luminosity to be *MJD* = $59052.8^{+0.8}_{-0.6}$. If we instead fit just the *g*-band data, we find a peak time of *MJD* = $59065.9^{+0.9}_{-0.8}$, suggesting that like some TDEs (Holoien et al. 2018, 2019b; Hinkle et al. 2021b) ASASSN-20hx may have peaked earlier in bluer bands, although we do not have early enough Swift coverage to test this directly.

ASASSN-20hx is the first ANT for which the early time rise was caught in an active TESS sector. We fit the early time rise as a power law with

$$f = z \text{ for } t < t_1, \text{ and} \tag{1}$$

$$f = z + h\left(\frac{t - t_1}{\text{observed days}}\right)^{\alpha} \text{ for } t > t_1 \tag{2}$$

This model fits for the zero-point z, the time of first-light t_1, a flux scale h, and the power-law index α. An MCMC fit yields best-fit parameters of $z = 12.1 \pm 1.0 \ \mu$Jy, $h = 32.5^{+3.5}_{-3.2} \ \mu$Jy, t_1(MJD) = 59022.8 ± 0.1, and $\alpha = 1.05 \pm 0.06$ and are shown in Figure 7. While the best-fit time of first light appears to be very close to the downlink gap, we reran the analysis with the
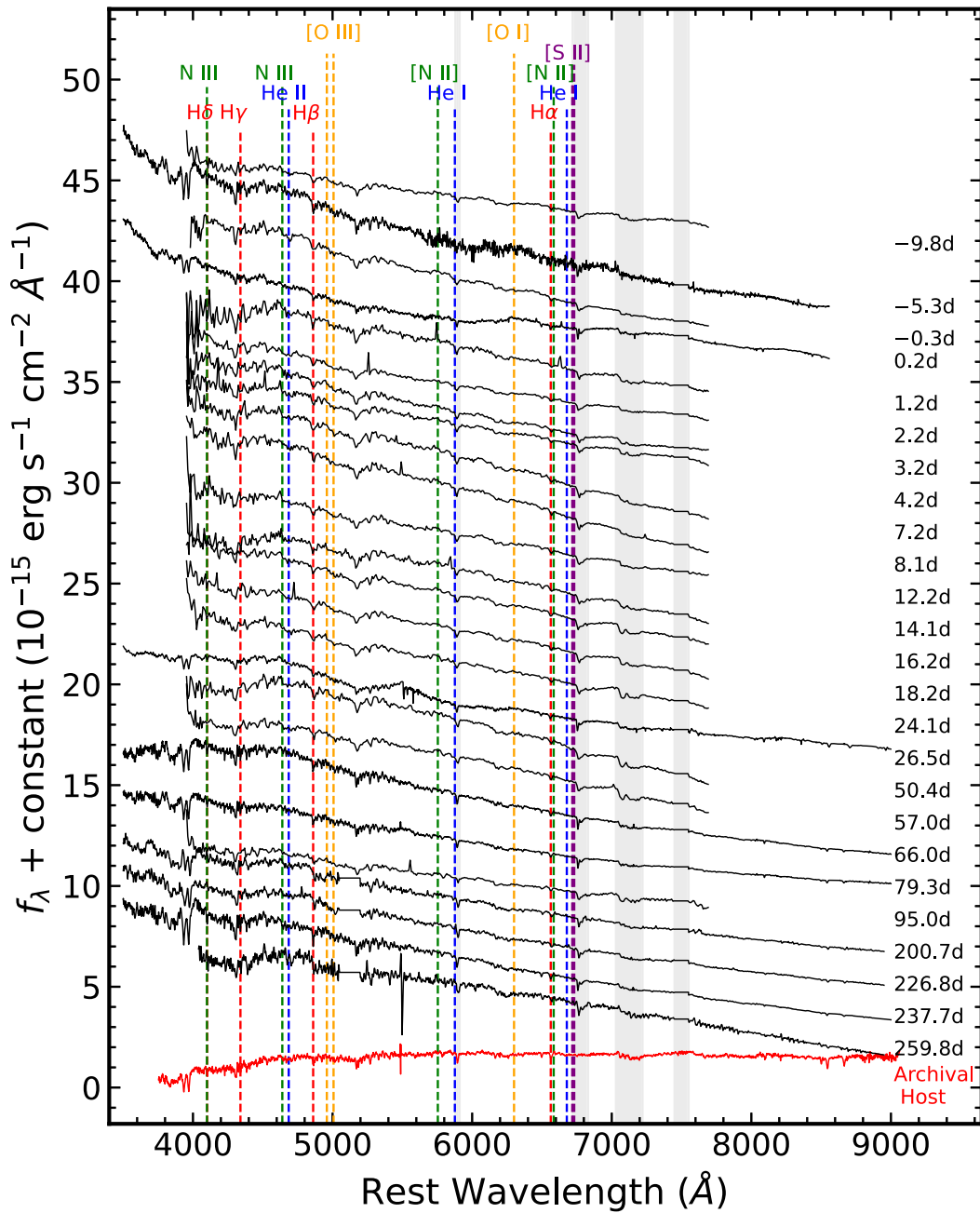
---

[25] https://www.cadc-ccda.hia-iha.nrc-cnrc.gc.ca/en/

Figure 6. Optical spectroscopic evolution of ASASSN-20hx spanning from 10 days prior to peak UV/optical emission (top) until 259 days after peak (bottom). These spectra are calibrated using the photometry presented in Figure 5 as well as the corresponding blackbody fits. The archival host spectrum from SDSS is shown in red at the very bottom. The vertical gray bands mark atmospheric telluric features. The strong telluric feature between ~7400–7550 Å and several artifacts in individual spectra have been masked. The vertical lines mark spectral features common in TDEs and AGNs, with hydrogen lines in red, helium lines in blue, nitrogen lines in green, sulfur lines in purple, and oxygen lines in orange.

(The data used to create this figure are available.)

first 6 hr of post-gap TESS data removed and found parameters consistent with the original fit. From Figure 7, we see that the light curve rises from the time of first light to the peak UV/optical bolometric luminosity in ~30 days, shorter than the rise to the peak time measured for ASASSN-19bt (Holoien et al. 2019c), and the limits on the rise times for PS18kh (Holoien et al. 2019a) and ASASSN-18pg (Holoien et al. 2020), but similar to the rise time for the TDE ASASSN-19dj (Hinkle et al. 2021b). From the best-fit time of first light, we find that

ASAS-SN discovered this transient just over two weeks after the beginning of the flare.

The best-fit power-law index of $\alpha = 1.05 \pm 0.06$ for the rise of ASASSN-20hx is consistent with the rise slope for the recurring partial TDE ASASSN-14ko although the rise time for ASASSN-14ko is much shorter at ~5 days (Payne et al. 2021). Conversely, the rise slopes of the TDEs ASASSN-19bt (Holoien et al. 2019a), ASASSN-19dj (Hinkle et al. 2021b), and ZTF19abzrhgq (AT2019qiz, Nicholl et al. 2020) are each consistent with a quadratic rise ($\alpha = 2$).
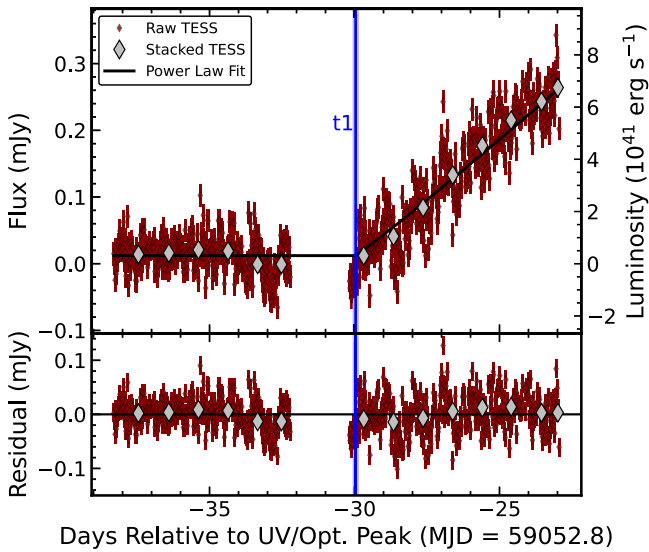
Figure 7. Top panel: stacked (silver) and raw (red) TESS light curve and best-fit power-law model in black. This power-law fit yields a time of first light of $t_1 = 59022.8 \pm 0.1$ and a power-law index of $\alpha = 1.05 \pm 0.06$. The blue line shows the fit time of first light with the uncertainty comparable to the line width. Bottom panel: residuals between the data and best-fit power-law model.

Under the assumption that ASASSN-20hx might be a TDE, we used the Modular Open-Source Fitter for Transients (MOSFiT; Guillochon et al. 2017; Mockler et al. 2019) to fit the host-subtracted light curves of ASASSN-20hx to estimate physical parameters of the star, SMBH, and the interaction. MOSFiT uses models with multiple physical parameters to generate bolometric light curves of a TDE, and computes single-filter light curves from the bolometric light curves that are then fit to the observed data. MOSFiT then finds the highest likelihood match of the various parameters for a given model using one of various sampling methods. We ran the MOSFiT TDE model in the nested sampling mode to account for the large number of observations in several photometric filters.

During initial testing of the MOSFiT fits to our data set, we found that MOSFiT preferred a black hole mass of $M_h \sim 10^6$ $M_\odot$. As this is nearly 2 orders of magnitude below the mass we estimated from the stellar mass of the host galaxy, we performed our final MOSFiT fits using a prior of $7 \leqslant \log(M_h) \leqslant 8.5$ on the mass of the SMBH. Figure 8 shows the MOSFiT multiband fits to the light curves of ASASSN-20hx.

MOSFiT is one of the only available tools for fitting TDE emission in detail, and appears to reproduce events like ASASSN-20hx, with relatively smooth light curves well. MOSFiT does a reasonable job of fitting the data throughout the event, both near the peak and at late times. Given the rapid rise of ASASSN-20hx relative to its long decay, the rise is not particularly well constrained by the MOSFiT model. The strong agreement between the late-time data and the model may suggest that if ASASSN-20hx is a TDE it may be predominantly accretion-powered.

Table 5 shows the median and 1%–99% range for the MOSFiT TDE model parameters. The model parameters are generally very well constrained, with statistical uncertainties from the fit being significantly smaller than the systematic uncertainties of the model (see Table 3 of Mockler et al. 2019). The black hole mass and stellar mass given by MOSFiT are log $(M_h/M_\odot) = 7.03 \pm 0.20$ and $M_\star = 0.36^{+3.89}_{-0.33} M_\odot$, respectively. This black hole mass is smaller than the value estimated from

scaling relations using our host stellar mass and is close to the lower bound of our prior constraints on the mass, which is perhaps unsurprising. The mass of the star is similar to the masses obtained for the TDEs modeled by Mockler et al. (2019). As expected from the long overall timescale for ASASSN-20hx and the relatively slow rise to the peak, MOSFiT prefers a fit in which the star was only partially disrupted in the encounter, with $b = 0.81$. However, for an interaction with a low-mass star and a b value less than 1, the systematic uncertainties on b are quite significant, and the model is consistent with both full disruption ($b < 1$) and minimal partial disruption ($b \ll 1$) scenarios.

We also performed fits without using our prior on the SMBH mass, and we find that the resulting light-curve fits are comparable to those from our constrained fit that are shown in Figure 8. Given that the fit is not clearly better when the SMBH mass is unconstrained, we determined that the results of our constrained fit are valid, and present those in full above. However, for the sake of clarity, we note that in the unconstrained fits the best-fit masses and b values are log $(M_h/M_\odot) = 6.23^{+0.23}_{-0.22}$, $M_\star = 0.50^{+1.84}_{-0.39} M_\odot$, and $b = 1.03^{+0.22}_{-0.88}$.

MOSFiT assumes that the observed TDE is predominantly tied to rapid circularization and accretion onto the SMBH. If we instead want to understand the emission of ASASSN-20hx near the peak in the context of a TDE powered by stream-stream collisions, we used TDEmass (Ryu et al. 2020). Unlike MOSFiT, TDEmass assumes that the UV/optical emission is shock-powered and extracts the SMBH and stellar mass based on the observed peak luminosity and temperature at peak. Using our peak luminosity of $(3.15 \pm 0.04) \times 10^{43}$ erg s^{-1} and temperature at peak of $22,800^{+910}_{-875}$ K, we obtain a SMBH mass of $9.1^{-1.0}_{+2.5} \times 10^5 M_\odot$ and a disrupted stellar mass of $0.62^{+0.05}_{-0.01}$ $M_\odot$. Given the stellar mass of the host galaxy, this SMBH mass is several orders of magnitude lower than expected. The disrupted stellar mass is consistent with other TDEs (Ryu et al. 2020) and consistent with the MOSFiT result.

The estimated SMBH masses from both MOSFiT and TDEmass are lower than the mass estimated from the host-galaxy mass and scaling relations. This may suggest that a TDE origin for ASASSN-20hx is disfavored. However, for the case of the MOSFiT model with a prior on mass, we find that, when incorporating uncertainties both on the scaling relations and the MOSFiT result, the SMBH masses are consistent to within $\sim 2\sigma$.

3.2. Radio Constraints

In addition to the optical light curve of ASASSN-20hx, we can compare the submillimeter limit we obtained with JCMT to radio observations of TDEs. At phases of ~ 245 and ~ 274 days from first light, ASASSN-20hx was not detected in the submillimeter, with 3σ upper limits of 8.9 mJy and 8.5 mJy, respectively. As most observations of TDEs occur in the radio rather than the submillimeter, we converted our 353 GHz flux to a 5 GHz flux for a more direct comparison (e.g., Alexander et al. 2020). To do this, we used the radio light curve of ZTF19aapreis from Cendes et al. (2021) as an approximate radio light-curve model for a normal TDE. We adopted the basic assumptions of $\nu_m = 0.1$ GHz and $p = 2.7$ from Cendes et al. (2021). For each epoch in their radio light curve, we used their measured ν_a and peak flux values to scale the expected radio/submillimeter SED. We then measured the flux ratio between the 5 GHz and 353 GHz at each epoch. Finally, we
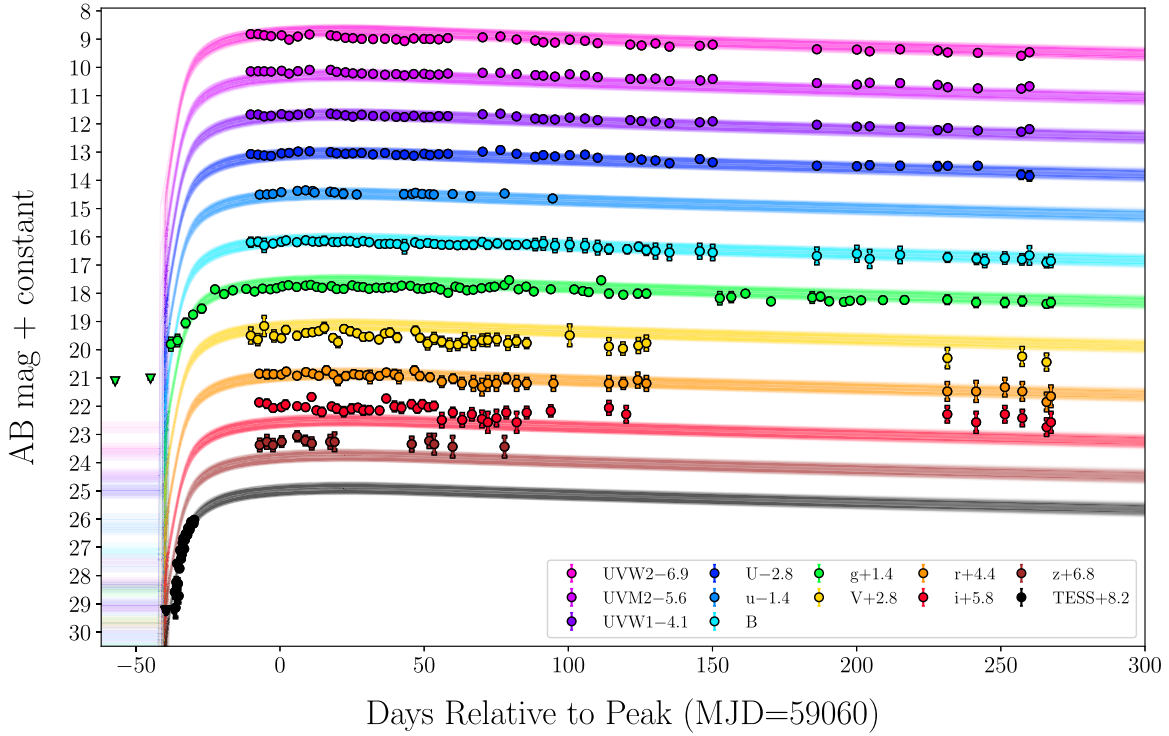
Figure 8. MOSFiT light curve fits and host-subtracted light curves. The 1%–99% range of fits for each filter are shown as shaded regions with the median fit shown as a solid line. All detections are plotted as circles with 3σ upper limits plotted as downward triangles. The colors match those of Figure 5.

Table 5
MOSFiT TDE Model Parameter Fits

Quantity	Value	Units
$\log R_{\mathrm{ph0}}$ (photosphere power-law constant)	$-0.74^{+0.40}_{-0.40}$	...
$\log T_{\mathrm{viscous}}$ (viscous delay timescale)	$-1.49^{+1.00}_{-1.00}$	days
b (scaled impact parameter β)	$0.81^{+0.89}_{-0.81}$	...
$\log M_h$ (SMBH mass)	$7.03^{+0.20}_{-0.20}$	$M_\odot$
$\log \epsilon$ (efficiency)	$-0.48^{+0.68}_{-0.68}$	...
l (photosphere power-law exponent)	$0.30^{+0.21}_{-0.21}$	...
$\log n_{\mathrm{H,host}}$ (local hydrogen column density)	$21.07^{+0.01}_{-0.01}$	cm^{-2}
$M_\star$ (stellar mass)	$0.36^{+3.89}_{-0.33}$	$M_\odot$
t_{exp} (time of disruption)	$-1.67^{+15.00}_{-15.02}$	days
$\log \sigma$ (model variance)	$-0.67^{+0.02}_{-0.02}$	...

Note. Best-fit values and 1%–99% ranges for the MOSFiT TDE model parameters. Units are listed where appropriate. The listed uncertainties include both statistical uncertainties from the fit and the systematic uncertainties listed in Table 3 of Mockler et al. (2019). The systematic error on b, of 0.88, is larger than our estimated value.

interpolated this scaling to find the factor needed to estimate at 5 GHz flux at the phase of our JCMT epoch. This yielded a conversion factor of $f_{353GHz}/f_{5GHz} = 0.0343$ for the JCMT epoch that occurred $\sim$245 days after first light and $f_{353GHz}/f_{5GHz} = 0.0317$ for $\sim$274 days after first light. Therefore, given our 353 GHz upper limit, we estimate limits of 259 mJy and 269 mJy at 5 GHz at the two epochs. At the distance of ASASSN-20hx, these correspond to a 5 GHz luminosity of 8.2×10^{39} erg s^{-1} and 8.5×10^{39} erg s^{-1}. These estimates are shown in Figure 9. While this estimate requires several assumptions about the type of transient and radio evolution, it is sufficient to show that ASASSN-20hx is considerably fainter than the jetted/relativistic TDEs Swift J2058+05 and
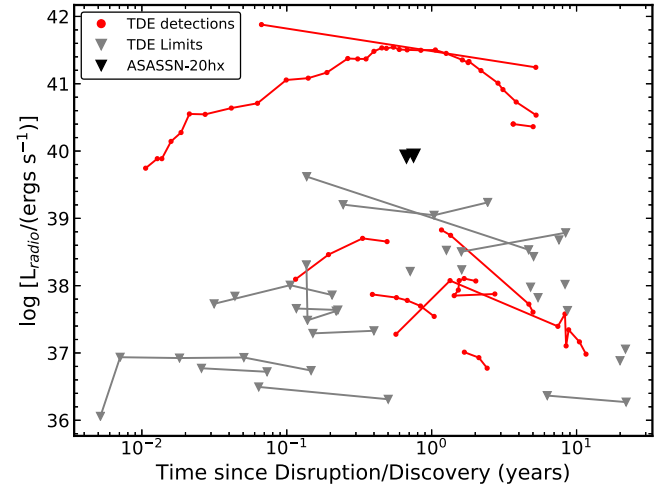
Figure 9. $\sim$5 GHz radio light curves of TDEs from Alexander et al. (2020). The red lines show detected radio emission from TDEs, and the gray lines show upper limits. The two black downward-facing triangles are the 3σ upper limits for the radio emission of ASASSN-20hx.

Swift J1644+57. This likely suggests that either ASASSN-20hx did not launch a strong jet or the jet was off-axis (Irwin et al. 2015; Yuan et al. 2016).

3.3. Spectra

The spectra of ASASSN-20hx exhibit a blue continuum and are devoid of any emission-line features. Indeed, even after subtracting the SDSS host spectrum from the various follow-up spectra, emission lines remain conspicuously absent. This type of evolution is unusual for both TDEs and AGN. TDEs commonly exhibit broad H emission (e.g., Holoien et al. 2014; Hung et al. 2020a; Holoien et al. 2020; Hinkle et al. 2021b),
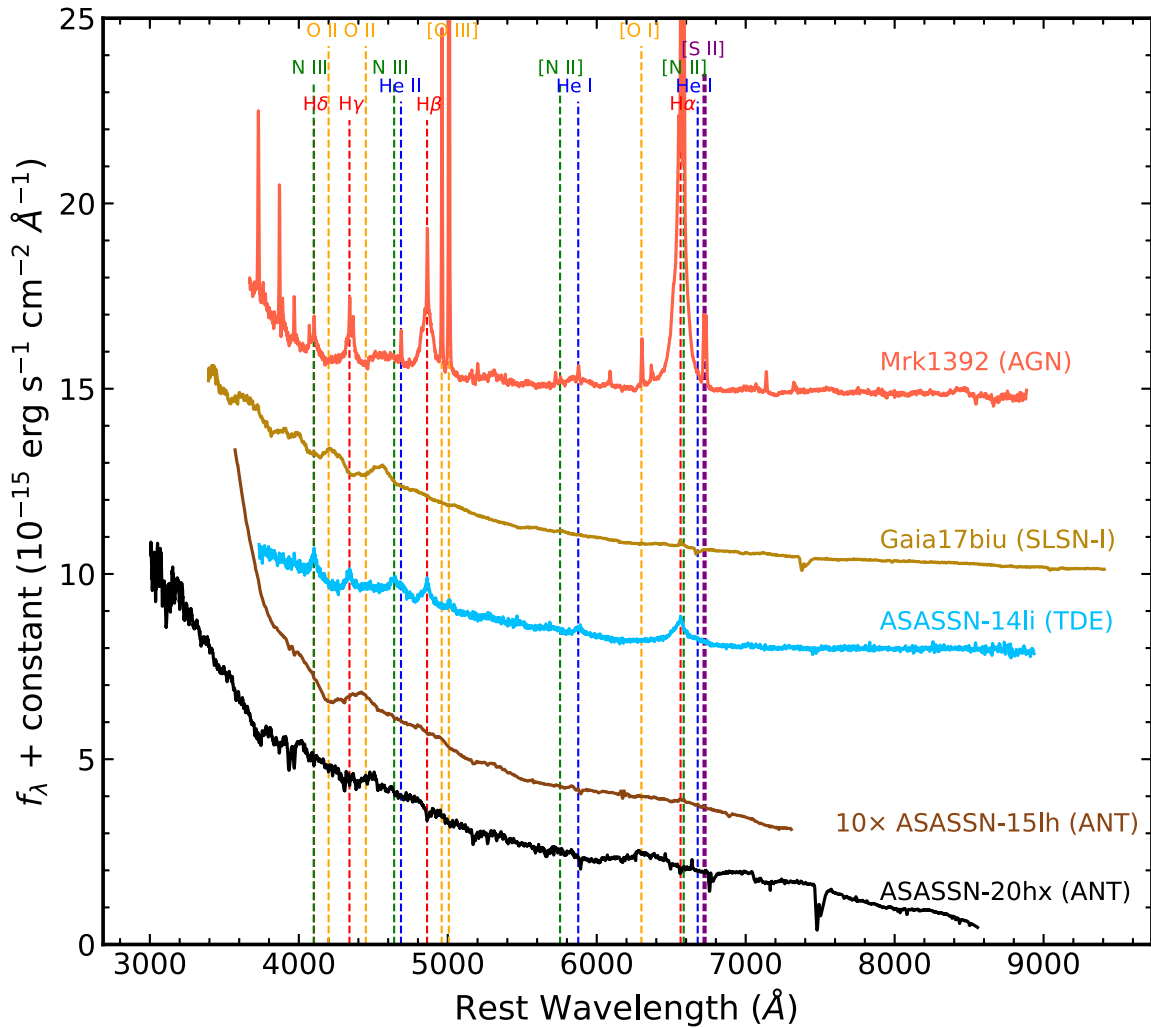
Figure 10. Spectrum of ASASSN-20hx as compared to the ANT ASASSN-15lh (brown line; Dong et al. 2016; Leloudas et al. 2016), the TDE ASASSN-14li (blue line; Holoien et al. 2016a), the SLSN-I Gaia17biu (golden line; Bose et al. 2018), and the Seyfert 1 Mrk1392 (red line; Adelman-McCarthy et al. 2006). The spectra of the transients are all selected to be near peak emission. The vertical lines mark spectral features common in TDEs, AGNs, and SLSNe with hydrogen lines in red, helium lines in blue, nitrogen lines in green, sulfur lines in purple, and oxygen lines in orange.

and many TDEs also show broad He lines (e.g., Blagorodnova et al. 2017; Wevers et al. 2019a; Hinkle et al. 2021b) and/or metal lines of O and N (Leloudas et al. 2019; van Velzen et al. 2021). None of these lines are present in the spectra of ASASSN-20hx at any point in the evolution. Conversely AGNs tend to have H lines that are somewhat narrower than those seen in TDEs at a given SMBH mass and luminosity along with narrow forbidden lines of O, N, and S (Baldwin et al. 1981; Veilleux & Osterbrock 1987).

Figure 10 shows a spectrum of ASASSN-20hx near the peak as compared to a well-studied TDE and a strong AGN. ASASSN-20hx shows none of the emission or absorption lines seen in these other classes of objects. Figure 10 also shows a spectrum of a SLSNe-I, which are largely featureless near the peak except for O II absorption (e.g., Gal-Yam 2012; Bose et al. 2018; Lunnan et al. 2020). This SLSN-I spectrum does not match the largely featureless nature of ASASSN-20hx, where no broad-line features are present. Additionally, we compare ASASSN-20hx to the ANT ASASSN-15lh (e.g., Dong et al. 2016; Leloudas et al. 2016). While significantly more luminous, ASASSN-15lh has a similarly featureless spectrum. In Figure 10, we see that ASASSN-20hx has even

fewer features than ASASSN-15lh, lacking the broad features near ~4300 Å. Even if ASASSN-20hx is an example of a new AGN rapidly turning on, the lack of hydrogen emission would be unusual (e.g., Trakhtenbrot et al. 2019b). The only obvious case in which an AGN would not show emission lines is a blazar (e.g., Paggi et al. 2014), although this is likely ruled out by the lack of detected submillimeter emission.

Figure 11 shows three high-SN, host-subtracted spectra from various phases in the evolution of ASASSN-20hx. None of the expected emission lines are visible in these deep spectra. The broad feature at ~6300 Å in the LRIS spectrum is not present in a SPRAT spectrum taken the same day, suggesting it is a reduction artifact caused by known issues with the red channel of LRIS at the time the spectrum was obtained. This artifact was accentuated by the blackbody scaling and host-subtraction procedures. In none of these spectra do we see evidence for lines consistent with a TDE, AGN, or SN origin.

We computed limits on the existence of Hα, He II λ4686, and He I λ10830 from our optical and NIR spectra to quantify the weakness of any line features. To do this, we followed the procedure of Leonard & Filippenko (2001) and Tucker et al. (2020), assuming a AGN-like line width of 2000 km s^{-1} and
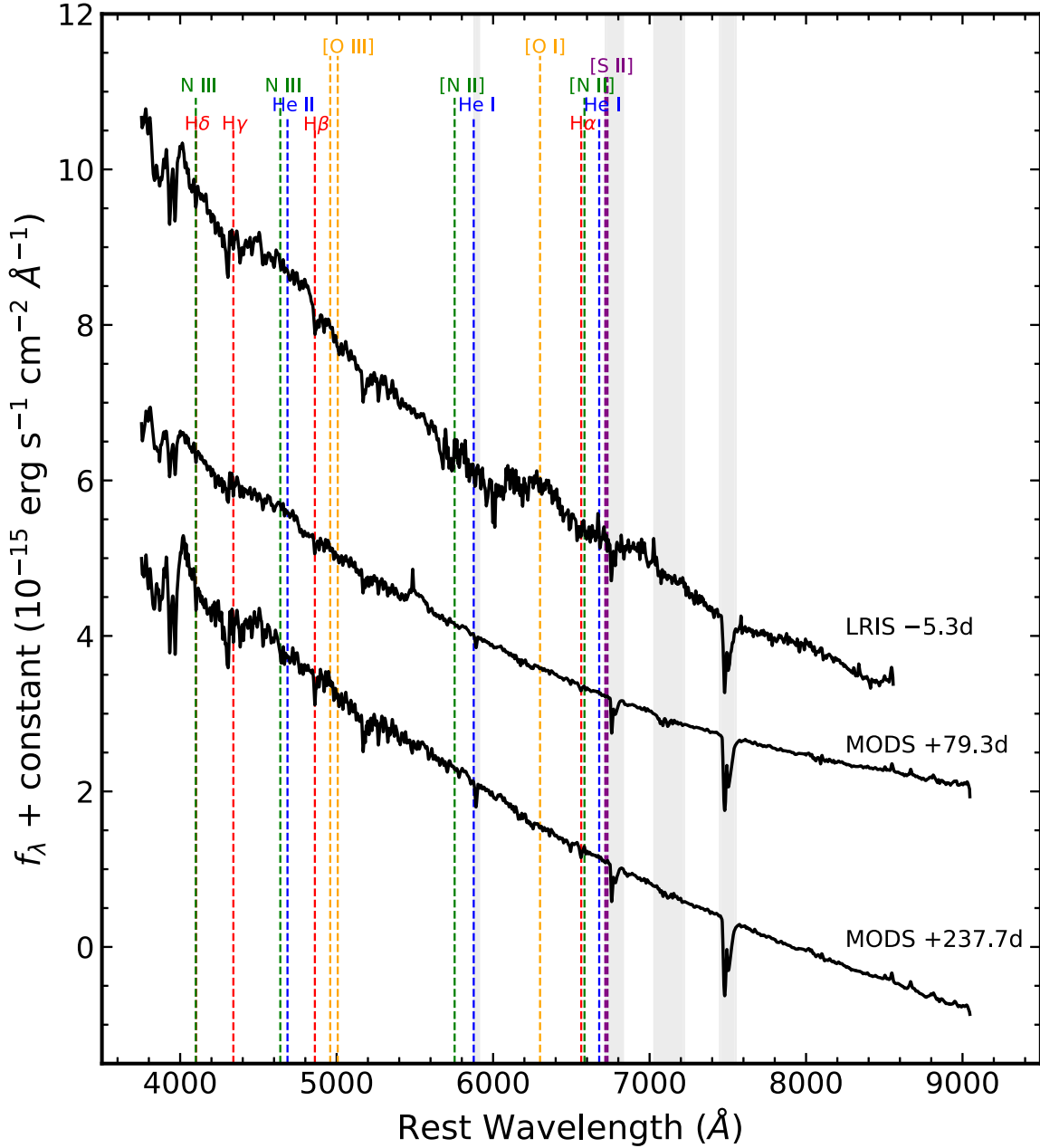
Figure 11. High-SN, host-subtracted spectra from LRIS and MODS at three phases throughout the evolution of ASASSN-20hx. The features near 6300 Å and 5500 Å in the LRIS and MODS spectra, respectively, are reduction artifacts that were accentuated by the blackbody scaling and host-subtraction procedures. The vertical gray bands mark atmospheric telluric features. The vertical lines mark spectral features common in TDEs and AGNs, with hydrogen lines in red, helium lines in blue, nitrogen lines in green, sulfur lines in purple, and oxygen lines in orange.

obtained 5σ flux limits as

$$F(5\sigma) = 5C_\lambda \Delta I \sqrt{W_{line} \Delta X} \qquad (3)$$

where C_λ is the continuum flux at wavelength λ, ΔI is the rms scatter around a normalized continuum, W_{line} is the width of the line profile, and ΔX is the pixel scale of the spectrum. The results are shown in Figure 12. The majority of the limits for both Hα and He II $\lambda4686$ are below $\sim 2 \times 10^{39}$ erg s^{-1}, one to two orders of magnitude less than the line emission typically seen in AGNs or TDEs (e.g., Bentz et al. 2010; Gezari et al. 2012; Holoien et al. 2019b; Neustadt et al. 2020). Additionally, the limits on Hα lie at a few percent of the Hα emission predicted from the correlation between X-ray luminosity and

Hα luminosity in AGNs from Shi et al. (2010). The limits on Hα luminosity are also much less than TDEs with H emission (e.g., Holoien et al. 2014, 2019a; Hinkle et al. 2021b). We also find that the NIR He I $\lambda10830$ emission is less than a percent of what is seen in known broad-line AGN. While the comparison samples used here are heterogeneous, they all illustrate that the limits on the line emission from ASASSN-20hx are very strong, with none of these lines approaching typical levels. The few epochs with larger limits on line luminosity have noticeable noise in their spectra or occur at the crossover regions in the spectrograph on which they were taken.

Given the lack of features in the optical spectra, we obtained a NIR spectrum, shown in Figure 13, to search for lines. Many
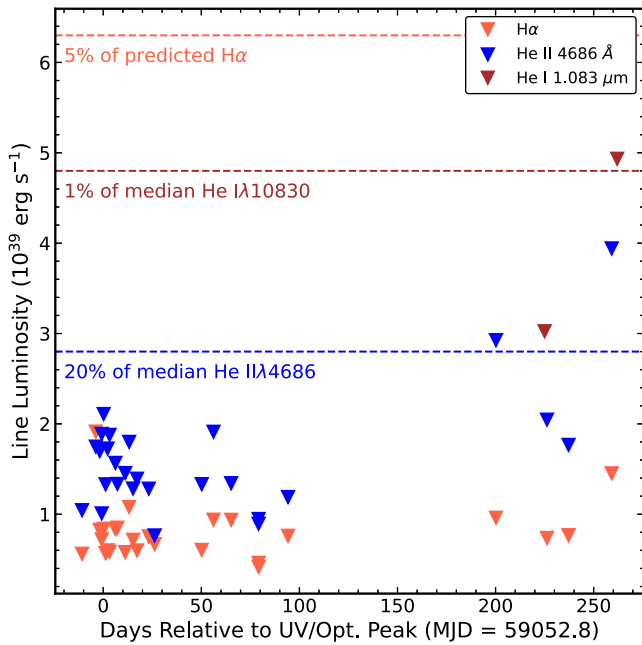
Figure 12. 5σ limits on the Hα, He IIλ4686, and He I λ10830 emission from ASASSN-20hx. The dashed red line indicates 5% of the expected Hα emission for an AGN with the X-ray luminosity of ASASSN-20hx using the correlation of Shi et al. (2010). The dashed blue line is 20% of the median He II λ4686 luminosity from the sample of Bentz et al. (2010). The dashed brown line is 1% of the median He I λ10830 luminosity from the sample of Landt et al. (2008). In the case of Hα and He I λ10830, the limits are at the level of a few percent or lower and at roughly the 10% level for He II λ4686.

of the H and He lines are more isolated in the NIR than in the optical. As with the optical spectra, there is no clear evidence for any H or He emission that might suggest an AGN origin for this transient. We also search for high-ionization coronal lines (e.g., Lamperti et al. 2017), but found no evidence for any of the lines commonly seen in AGN.

3.4. Spectral Energy Distribution

The SED of ASASSN-20hx is shown in Figure 14. These data are taken at a phase of roughly 250 days after the peak, where we have X-ray, UV/optical, and submillimeter constraints on the transient emission. The SED shows that the UV/optical emission from ASASSN-20hx is dominant over the X-ray emission and that the total emission is far below the Eddington luminosity for the expected black hole mass of the host galaxy. While the dominance of the UV/optical emission and the good fit of a blackbody SED are similar to known TDEs (e.g., Holoien et al. 2014, 2016a; van Velzen et al. 2021), they are also qualitatively similar to unobscured AGNs over this wavelength range (e.g., Assef et al. 2010).

Given the dominance of the UV/optical emission from ASASSN-20hx, we fit it as a blackbody, similar to many previous TDEs and nuclear flares (Hinkle et al. 2021a). Figure 15 shows the blackbody model fits in terms of luminosity, radius, and temperature for ASASSN-20hx compared to the well-studied TDEs ASASSN-19dj (light blue line; Hinkle et al. 2021b), ZTF19abzrhgq (AT2019qiz; brown line; Nicholl et al. 2020), ASASSN-18ul (AT2018fyk, orange line; Wevers et al. 2019a; A. V. Payne et al. 2022, in preparation), ASASSN-18pg (purple line; Holoien et al. 2020), ASASSN-15oi (pink line; Holoien et al. 2018), ASASSN-14li (gray line; Brown et al. 2017), and iPTF16fnl (dark blue line;

Blagorodnova et al. 2017; Brown et al. 2018) and to the nuclear transients ASASSN-18el (red line; Trakhtenbrot et al. 2019a), ASASSN-17cv (AT2017bgt, green line; Trakhtenbrot et al. 2019b), and ASASSN-18jd (gold line; Neustadt et al. 2020). ASASSN-20hx is among the least luminous of the well-studied nuclear transients, with a peak luminosity of $(3.15 \pm 0.04) \times 10^{43}$ erg s^{-1}. Using the SMBH mass computed from scaling relations, the peak luminosity corresponds to an Eddington ratio of $\sim 3 \times 10^{-3}$, roughly 100 times less than typical TDEs (Wevers et al. 2017) and consistent with the lower end of the distribution of optically selected AGNs (Kauffmann & Heckman 2009). This peak luminosity is comparable to the TDEs ZTF19abzrhgq (AT2019qiz; Nicholl et al. 2020) and iPTF16fnl (Blagorodnova et al. 2017; Brown et al. 2018). Unlike these faint TDEs, the decline in the bolometric luminosity of ASASSN-20hx is quite slow. The decline slope of the bolometric luminosity of ASASSN-20hx appears similar to the other ANTs in our sample, which are all flatter than the TDE comparison sample.

The blackbody radius of ASASSN-20hx is large compared to the well-studied TDEs, but it is similar to the ANTs in the comparison sample. Unlike many TDEs with a well-sampled late-time evolution (e.g., Hinkle et al. 2020a, 2021b; van Velzen et al. 2021), the blackbody radius of ASASSN-20hx does not decrease significantly at late times. This relatively flat late-time radius evolution is similar to other AGN-related nuclear flares (e.g., Hinkle et al. 2021a).

The effective temperature of ASASSN-20hx is moderately cool compared to other TDEs and ANTs, on the order of $\sim$21,000 K. Nonetheless, the temperature of ASASSN-20hx is similar to some nuclear flares like ASASSN-18el. Interestingly, the blackbody temperature of ASASSN-20hx is most similar to TDEs exhibiting strong H emission (Holoien et al. 2019a, 2019b; Hung et al. 2020a) although ASASSN-20hx does not display H emission. Like the TDEs and nuclear flares in our comparison sample, ASASSN-20hx displays a flat temperature throughout its evolution, with only a small decrease soon after the peak.

Finally, with bolometric light curves, we can compare the light-curve evolution of ASASSN-20hx to other well-studied TDEs and nuclear flares using the method of Hinkle et al. (2020a). By measuring the peak UV/optical luminosity and comparing it to the decline rate, we can see where ASASSN-20hx lies relative to TDEs of similar luminosities as shown in Figure 16. The first striking point is that ASASSN-20hx is less luminous than any of the TDEs in this sample. For the fundamental plane distance of 55.6 Mpc (Saulder et al. 2016), this luminosity difference would be even stronger. Unlike the two faintest TDEs to date, ASASSN-20hx does not fade quickly, declining by only $\sim$0.1 dex in luminosity over the first forty days after the peak. While much less luminous, this decline rate is similar to the other ANTs. The fact that ASASSN-20hx lies far from the known TDE relationship and occupies a region of decline rate space similar to AGN-related transients strongly suggests that it is not a normal TDE. As suggested by its similarities to ASASSN-18el in Figure 15, ASASSN-20hx lies close to this ANT in Figure 16.

3.5. X-Rays

While the host galaxy of ASASSN-20hx showed weak X-ray emission prior to the current outburst, the X-ray emission associated with the transient is roughly an order of magnitude
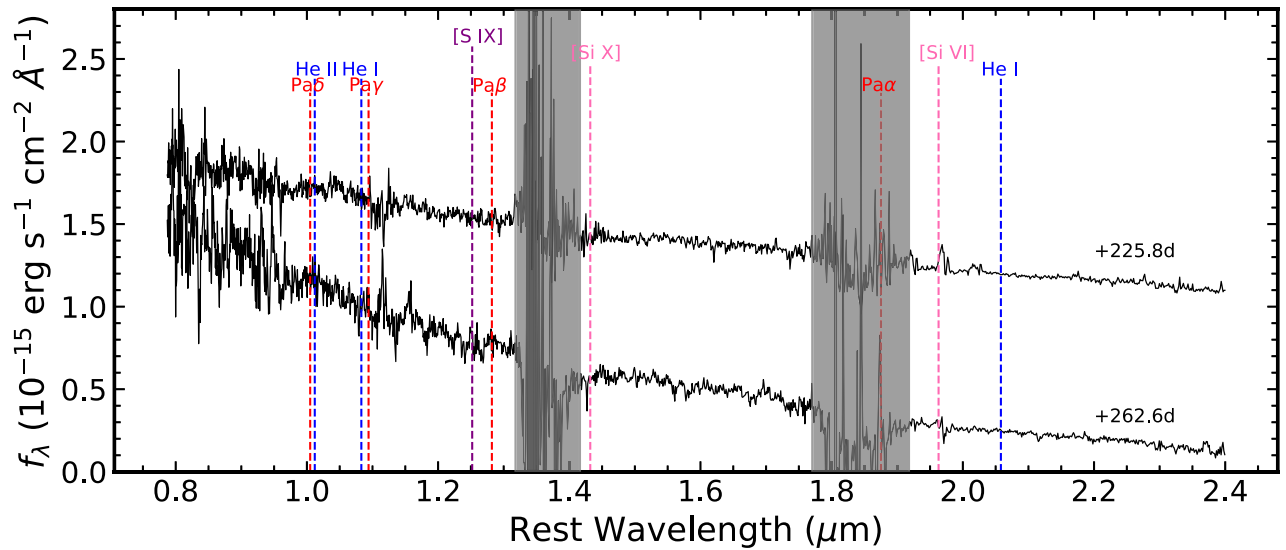
Figure 13. NIR spectra of ASASSN-20hx obtained with IRTF 225.2 days after peak. The vertical gray bands mark strong atmospheric telluric features. The vertical lines mark spectral features common in AGN, with hydrogen lines in red and helium lines in blue. Coronal silicon and sulfur lines are shown in pink and purple, respectively. The spectra have been binned to ∼5 Å bins.
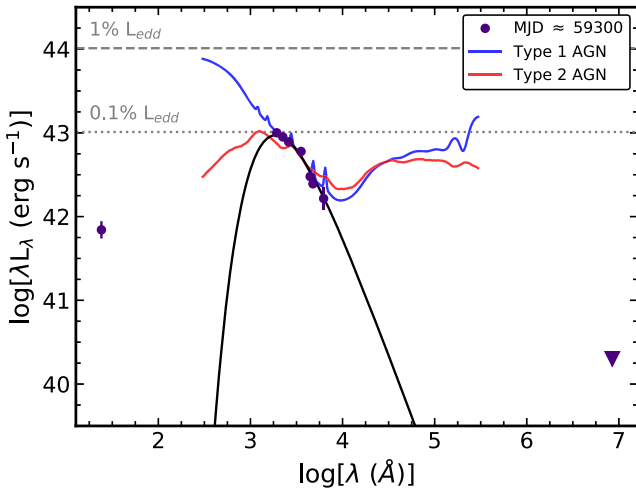

Figure 14. Spectral energy distribution of ASASSN-20hx at MJD ∼53900, at roughly 250 days after peak. The black line is the corresponding best-fitting blackbody model at this phase. The downward-facing triangle shows the 3σ upper limit on the submillimeter emission at the measured frequency. The horizontal gray dashed and dotted lines show 1% and 0.1% of the Eddington luminosity for a SMBH of $10^{7.9}\,M_\odot$, respectively. The blue and red lines show typical SEDs of Type 1 and Type 2 AGNs, respectively, from Assef et al. (2010) normalized to the ASASSN-20hx blackbody fit at the U band.

higher. In Figure 17 (top panel), we show the X-ray light curve as derived from the Swift and NICER observations. To estimate the X-ray luminosity, we converted the extracted count rate into flux using WebPIMMS[26] and assumed an absorbed power-law model with the average photon indices derived from our fits.

We analyzed the Swift and NICER spectra using the X-ray spectral fitting program XSPEC version 12.10.1f (Arnaud 1996), and chi-squared statistics. While we fit the NICER spectra individually, it was necessary to stack the Swift observations to get adequate S/N for spectral fits. Each of the spectra was well fit by an absorbed power law. The fits did not require additional absorption beyond the Galactic contribution, so all of the column densities were frozen at the Galactic value of 2.0×10^{20} cm^{-2}. We show the resulting photon indices from these spectral fits in the bottom panel of Figure 17.

Throughout the evolution of ASASSN-20hx, the merged Swift spectra and individual NICER spectra are best fit by an absorbed power-law model. In a few NICER spectra, there was marginal evidence for a blackbody component with kT ∼0.035 keV and a radius of ∼5×10^{11} cm. However, as this additional component is only needed for a small number of spectra and at moderate significance, we do not explore it further. In Table 6, we give the best-fit photon indices from our spectral fits.

For Swift the average photon index was $\Gamma = 2.24$, and for NICER, it was $\Gamma = 2.61$, although they are largely consistent within the uncertainties for the overlapping data. The presence of power-law X-ray emission is unlike many X-ray-luminous TDEs (e.g., ASASSN-14li, ASASSN-15oi, ASASSN-19dj; Brown et al. 2017; Holoien et al. 2018; Kara et al. 2018; Hinkle et al. 2021b), and is more consistent with an AGN scenario. The average photon index derived for ASASSN-20hx is typical of unobscured AGNs (Ricci et al. 2017).

The first X-ray observation of ASASSN-20hx was taken using the Swift-XRT roughly 3 days before the peak UV/optical emission (MJD = 59052.4). During this observation, ASASSN-20hx showed strong X-ray emission at a luminosity of ∼2×10^{42} erg s^{-1}. This is higher than many TDEs in the early phases of their evolution (Auchettl et al. 2017), but is similar to or less than the X-ray luminosities of other nuclear flares that have been suggested to be associated with AGN activity, such as ASASSN-18jd (Neustadt et al. 2020), ASASSN-17cv (AT2017bgt; Trakhtenbrot et al. 2019b), and several transients in the narrow-line Seyfert 1 galaxies (Frederick et al. 2020).

Unlike many other nuclear transients, such as ASASSN-18jd (Neustadt et al. 2020), ASASSN-18ul (AT2018fyk; Wevers et al. 2019a), and ASASSN-15oi (Gezari et al. 2017), the X-ray emission of ASASSN-20hx showed little variability over the

---
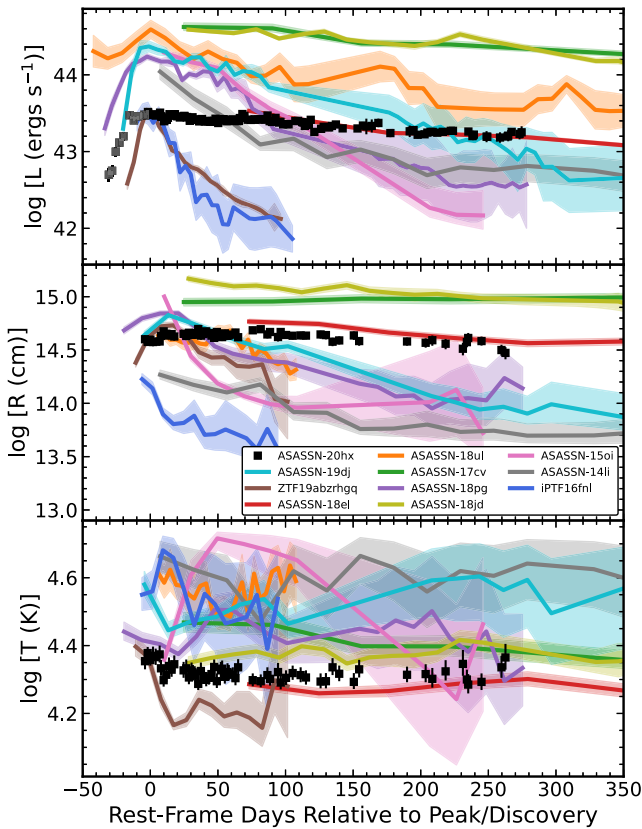
Figure 15. Evolution of the UV/optical blackbody luminosity (top panel), radius (middle panel), and temperature (bottom panel) for ASASSN-20hx (black squares) and a comparison sample of TDEs and ANTs. The lines are smoothed over the individual epochs by linearly interpolating to a time-series with the same length as the original coverage, but with half the number of points. Time is in rest-frame days relative to the peak luminosity for the objects discovered prior to peak (ASASSN-19dj, ASASSN-18ul, ZTF19abzrhgq, ASASSN-18pg, and iPTF16fnl), and relative to discovery for those that were not (ASASSN-18el, ASASSN-17cv, ASASSN-18jd, ASASSN-15oi, and ASASSN-14li). The gray squares for ASASSN-20hx indicate where data has been bolometrically corrected using the ASAS-SN g-band light curve assuming the temperature from the first Swift epoch was constant.

Figure 16. The peak luminosity vs. the decline rate of various TDEs and other nuclear outbursts. The decline rate ΔL_{40} is defined as the difference between the log of the peak luminosity and the log of the luminosity at 40 days after the peak. The squares and circles correspond to the various classes of objects in Hinkle et al. (2020a, 2021a), and the diamonds are events interpreted as AGN flares. The black solid line is the best-fit line for the TDEs, and the dashed black lines are the allowed range of uncertainty from the best-fit line. ASASSN-20hx lies well below the TDE relationship and is more consistent with the decline rates of the non-TDE nuclear transients.

first ∼100 days after the peak, varying between ∼$10^{42.0}$–$10^{42.2}$ erg s^{-1}. Unlike typical X-ray-luminous TDEs like ASASSN-14li (Holoien et al. 2016a) and ZTF19aapreis (AT2019dsg; van Velzen et al. 2021), the X-ray luminosity of ASASSN-20hx did not decrease significantly over the first ∼200 days after the peak. Using only the X-ray emission of ASASSN-20hx, we find an Eddington ratio of ∼3×10^{-4}, roughly 5 orders of magnitude higher than the Eddington ratio of Sgr A* computed from X-ray emission during flaring activity (Zhang et al. 2017).

The second panel of Figure 17 shows the evolution of the X-ray hardness ratio HR = (H−S)/(H+S), defining the hard (H) and soft (S) bands as 2–10 keV and 0.3–2 keV, respectively. ASASSN-20hx shows little variability in its hardness, with a HR range of roughly −0.8 to −0.3, excluding some individual NICER epochs with hardness ratios around zero. As the X-ray emission begins to fade toward ∼200 days after the peak, the hardness ratios increase slightly, but still remain below zero. The hardness ratios of ASASSN-20hx are generally consistent with AGNs (Auchettl et al. 2018) and are slightly harder than most TDEs (Auchettl et al. 2017, 2018; Hinkle et al. 2021b).

In the X-ray evolution of ASASSN-20hx, the HR and the X-ray luminosity evolve slowly with time. They seem to follow a weak inverse relationship, where the X-ray emission becomes harder as the luminosity of the source fades. This relationship is shown in Figure 18. Albeit much weaker for ASASSN-20hx, this evolution is consistent with what is seen in highly variable, X-ray bright AGNs (Auchettl et al. 2018) and some TDEs like ASASSN-19dj (Hinkle et al. 2021b).

Figure 19 shows the X-ray luminosity of ASASSN-20hx compared to the well-studied TDEs ASASSN-14li (Brown et al. 2017), ASASSN-15oi (Holoien et al. 2018), ASASSN-18ul (AT2018fyk; Wevers et al. 2019a, A. V. Payne et al. 2022, in preparation), ASASSN-19dj (Hinkle et al. 2021b), and ZTF19aapreis (AT2019dsg; van Velzen et al. 2021; K. Auchettl et al. 2022, in preparation) and to the nuclear transients ASASSN-17jz (Holoien et al. 2021), ASASSN-18el (Trakhtenbrot et al. 2019a; J. T. Hinkle et al. 2022, in preparation), ASASSN-18jd (Neustadt et al. 2020), and ZTF19abvgxrq (AT2019pev; Frederick et al. 2020; K. Auchettl et al. 2022, in preparation). The X-ray luminosity of ASASSN-20hx NUV/optical peak is below the median luminosity seen for X-ray bright TDEs and ANTs, but still higher than some like ASASSN-19dj. Many TDEs and ANTs show a late-time rebrightening period in their X-ray light curves, particularly notable for ASASSN-15oi, ASASSN-18el, and ASASSN-19dj. Over the roughly 275 days studied here for ASASSN-20hx, we see no evidence of such a feature. Indeed, the X-ray evolution is largely dissimilar to all other objects in our comparison sample. ASASSN-14li and ZTF19aapreis/ AT2019dsg both show monotonically declining X-ray light curves somewhat like ASASSN-20hx, but at much higher peak luminosities and different decline rates. Much like the other multiwavelength properties of ASASSN-20hx, the X-rays do not neatly agree with observations of known TDEs or AGN flares.
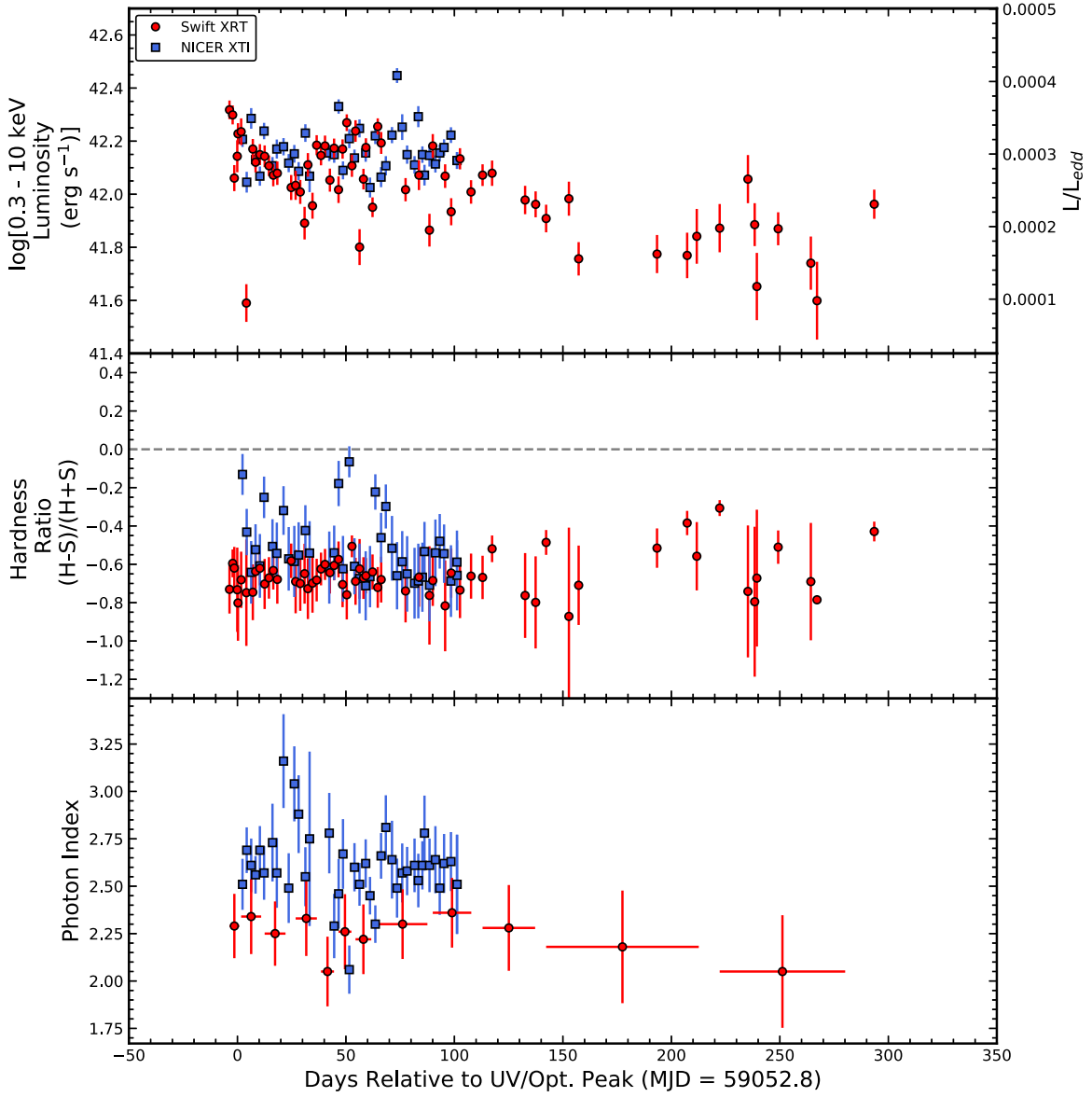
Figure 17. X-ray luminosity (top panel), hardness ratio (middle panel), and photon index (bottom panel) of ASASSN-20hx measured with Swift (red circles) and NICER (blue squares). We define hard counts H as the number of counts in the 2–10 keV range and soft counts S are the number of counts in the 0.3–2 keV range, with a gray dashed line marking zero. The hardness ratio is defined as (H−S)/(H+S).

Table 6
X-Ray Photon Indices

MJD	MJD Range	Γ	Γ Error	Satellite
59051.38	2.23	2.29	0.17	Swift
59055.14	⋯	2.51	0.13	NICER
59057.08	⋯	2.69	0.12	NICER
⋯	⋯	⋯	⋯	⋯
59177.90	12.11	2.28	0.23	Swift
59230.25	35.17	2.18	0.30	Swift
59303.98	28.92	2.05	0.30	Swift

Note. X-ray photon indices from the fits to the individual NICER spectra or the stacked Swift spectra. The MJD range indicates the length in time over which the Swift spectra were stacked.

(This table is available in its entirety in machine-readable form.)

Table 7
AGN versus TDE Properties of ASASSN-20hx

Property	ASASSN-20hx obs.	AGN/TDE like
$\log(M_{BH}) < 8\,M_{\odot}$	Yes	TDE
$\sigma_{H\beta} < 2000$ km s^{-1}	N/A	N/A
Fe II Emission	No	TDE
O III/$H\beta < 3$	Yes	AGN
$\Delta(g-r) \sim 0$	Yes	TDE
UV-bright	Yes	TDE
X-Ray Power Law	Yes	AGN
$W1 - W2 > 0.7$ mag	No	TDE
Rebrightening	No	TDE

Note. Properties to differentiate between TDEs and AGN flares, inspired by the classification scheme of Frederick et al. (2020). Based on whether or not ASASSN-20hx shows a given property, the final column indicates if this behavior is more AGN-like or TDE-like.

Table 8
Spectroscopic Observations of ASASSN-20hx

MJD	UTC Date	Telescope	Instrument	Rest Wavelength Range (Å)	Exposure Time (s)
59043.0	2020 July 13.0	Liverpool 2 m Telescope	SPRAT	3954–7863	1×900
59047.5	2020 July 17.5	Keck I 10 m Telescope	LRIS	3024–8557	$1 \times 600 + 1 \times 1200$
59052.0	2020 July 22	Liverpool 2 m Telescope	SPRAT	3981–7863	1×800
59052.5	2020 July 22.5	Keck I 10 m Telescope	LRIS	3006–8557	2×950
59053.0	2020 July 23.0	Liverpool 2 m Telescope	SPRAT	3954–7863	1×800
59054.0	2020 July 24.0	Liverpool 2 m Telescope	SPRAT	3954–7863	1×800
59055.0	2020 July 25.0	Liverpool 2 m Telescope	SPRAT	3954–7863	1×800
59056.0	2020 July 26.0	Liverpool 2 m Telescope	SPRAT	3954–7863	1×800
59057.0	2020 July 27.0	Liverpool 2 m Telescope	SPRAT	3954–7863	1×800
59060.0	2020 July 30.0	Liverpool 2 m Telescope	SPRAT	3954–7863	1×800
59060.9	2020 July 30.9	Liverpool 2 m Telescope	SPRAT	3954–7863	1×800
59065.0	2020 August 4.0	Liverpool 2 m Telescope	SPRAT	3954–7863	1×800
59066.9	2020 August 5.9	Liverpool 2 m Telescope	SPRAT	3954–7863	1×1200
59069.0	2020 August 8.0	Liverpool 2 m Telescope	SPRAT	3954–7863	1×1200
59071.0	2020 August 10.0	Liverpool 2 m Telescope	SPRAT	3954–7863	1×1200
59076.9	2020 August 15.9	Liverpool 2 m Telescope	SPRAT	3954–7863	1×1200
59079.3	2020 August 18.3	Keck I 10 m Telescope	LRIS	3340–9901	3×1050 (blue), 3×970 (red)
59103.2	2020 September 11	Large Binocular Telescope 8.4 m	MODS	3443–9048	3×1200
59109.8	2020 September 17.8	Liverpool 2 m Telescope	SPRAT	3954–7863	2×1200
59118.8	2020 September 26.8	Liverpool 2 m Telescope	SPRAT	3954–7863	2×1200
59132.1	2020 October 10	Large Binocular Telescope 8.4 m	MODS	3443–9048	3×1200
59132.8	2020 October 10.8	Liverpool 2 m Telescope	SPRAT	3954–7863	2×1200
59147.8	2020 October 25.8	Liverpool 2 m Telescope	SPRAT	3954–7863	2×1200
59253.6	2021 February 8.6	University of Hawaii 88-in Telescope	SNIFS	3347–8950	1×2700
59278.6	2021 March 5.6	NASA Infrared Telescope Facility	SpeX	7871–23993	24×50
59279.6	2021 March 6.6	University of Hawaii 88-in Telescope	SNIFS	3347–8950	1×2700
59290.5	2021 March 17	Large Binocular Telescope 8.4 m	MODS	3443–9048	4×900 s
59312.6	2021 April 8.6	University of Hawaii 88-in Telescope	SNIFS	4040–8950	1×2700
59315.4	2021 April 11.4	NASA Infrared Telescope Facility	SpeX	7871–23993	8×200

Note. Modified Julian Day, calendar date, telescope, instrument, wavelength range, and exposure time for each of the spectroscopic observations obtained of ASASSN-20hx for the initial classification and during our follow-up campaign. For some of the Keck/LRIS spectra, the red and blue sides have slightly different exposure times due to the very different readout times of the two chips. The two LT/SPRAT spectra taken on the same day as the Keck/LRIS and LBT/MODS spectra are not shown in Figure 6.

4. Discussion

ASASSN-20hx is a unique transient and perhaps the most clearly ambiguous of the growing class of ANTs. Much like other objects in this class, such as ASASSN-18jd (Neustadt et al. 2020), ASASSN-18el (Trakhtenbrot et al. 2019a), ASASSN-17cv (AT2017bgt; Trakhtenbrot et al. 2019b), and ZTF19aaiqmgl (AT2019avd; Frederick et al. 2020; Malyali et al. 2021), ASASSN-20hx shares some characteristics with both known TDEs and AGN. In Figures 15 and 16, we have compared the blackbody evolution and the decline rate to various well-studied TDEs and ANTs. Throughout the rest of this section, we will examine the properties of ASASSN-20hx as compared to other types of nuclear transients.

4.1. TDE-like Features of ASASSN-20hx

One of the key features of ASASSN-20hx that made it a strong candidate for a TDE based on its early evolution (Hinkle et al. 2020b) was the strong UV emission and blue colors. While less luminous than most TDEs, the UV emission from ASASSN-20hx was still substantial, with $M_{UV} \sim -18.6$ mag near the peak. The SED of ASASSN-20hx is well fit by a blackbody, similar to many TDEs (e.g., Hinkle et al. 2020a; van Velzen et al. 2021). The blackbody temperature of ASASSN-20hx is roughly 21,000 K throughout its evolution,

which is cooler than many TDEs, but still consistent with the larger population. Like most TDEs, the temperature of ASASSN-20hx stays relatively constant over time.

The peak luminosity of ASASSN-20hx of $(3.15 \pm 0.04) \times 10^{43}$ erg s^{-1} is very low for a TDE. Only iPTF16fnl (Blagorodnova et al. 2017) and ZTF19abzrhgq (AT2019qiz; Nicholl et al. 2020) have similar luminosities, but both of these TDEs fade quickly after their peaks (see Figure 16). While at a similar peak luminosity, ASASSN-20hx fades very slowly after its peak. In contrast, the decline rate of ASASSN-20hx is slower than any TDE included in the sample of Hinkle et al. (2020a).

The UV/optical light-curve evolution of ASASSN-20hx is similar to some TDEs in that the overall shape is quite smooth, although there are hints of weak short-term variability in the light curves. Additionally it is worth noting that some TDEs, like PS18kh (Holoien et al. 2019a; van Velzen et al. 2019), do show variability and moderate rebrightening episodes. The long-lived, flat UV/optical light curve without a significant initial decay is similar to the predictions for TDEs on more massive SMBHs (Mummery 2021).

ASASSN-20hx is one of the few nuclear transients where the slope of the initial flux increase can be measured. All of the TDEs for which such a fit has been possible (ASASSN-19bt, ASASSN-19dj, and ZTF19abzrhgq) have a flux $\propto t^2$ initial rise (Holoien et al. 2019c; Nicholl et al. 2020; Hinkle et al. 2021b),
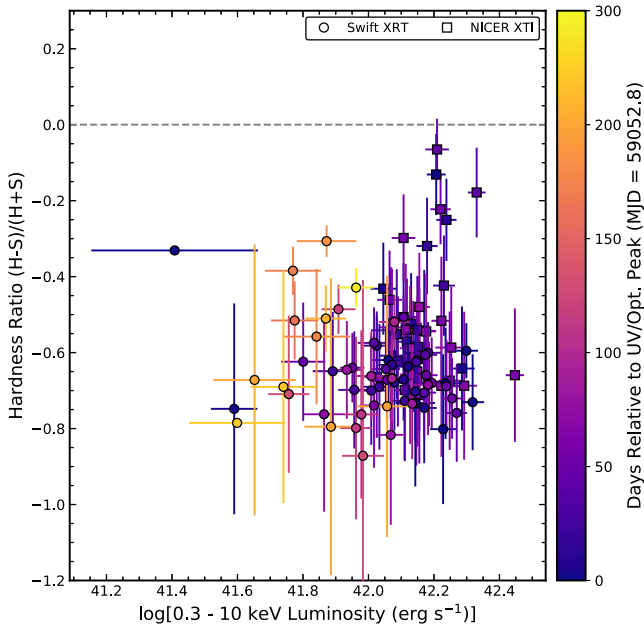
Figure 18. Hardness ratio as a function of X-ray luminosity as measured by Swift (circles) and NICER (squares) for the detections only. While the overall trend is small, as ASASSN-20hx becomes brighter, the X-ray emission becomes softer. This behavior is similar to that seen in X-ray bright AGNs (Auchettl et al. 2018). The color bar on the right indicates the phase relative to the UV/optical peak, with darker colors indicating earlier times.

while the flux of ASASSN-20hx rises linearly with time. However, the transient ASASSN-14ko, which is presently interpreted as a repeating partial TDE (Tucker et al. 2021; Payne et al. 2021, 2022) also shows a linear rise in its TESS light curve. The overall time for ASASSN-20hx to reach its peak UV/optical emission is similar to typical TDEs.

Next, we can compare the host galaxy of ASASSN-20hx to other TDE hosts. As shown in Figure 2, the host galaxy has less evidence of recently formed stars than many TDE hosts. As with most TDE hosts, the archival optical emission is nonvariable and shows no evidence of previous outbursts (see Figures 3 and 4). The SMBH mass derived from scaling relations for the host galaxy is $10^{7.9} M_\odot$, which is higher than most TDEs and very close to the point where the observable TDE rate begins to decrease rapidly (Kochanek 2016; van Velzen 2018; Wevers et al. 2019b).

The lack of broad spectral lines is odd for the TDE scenario. While various lines are seen at differing strengths in TDEs (e.g., Leloudas et al. 2019; van Velzen et al. 2021), H or He lines are almost always seen. In only one case, PS1-11af (Chornock et al. 2014), a TDE did not exhibit significant line emission. However, spectra were only obtained for PS1-11af near the peak emission, so we do not know if lines appeared later. It is possible to delay the production of strong lines (Roth & Kasen 2018), which has been observed for the TDE ASASSN-19dj (e.g., Hinkle et al. 2021b). This could explain the lack of emission lines, but lines typically appear relatively quickly after the peak (∼30 days), whereas ASASSN-20hx is still devoid of emission lines after a year.

The X-ray emission of ASASSN-20hx is also unlike any other TDE, starting with the fact that it is best fit by a power law rather than a blackbody. This is uncommon for TDE X-ray spectra (Auchettl et al. 2017). However, Mummery & Balbus (2021) suggest that TDEs on more massive SMBHs should

show nonthermal X-ray spectra and evolve more slowly, much like the observed behavior of ASASSN-20hx. While the hardness ratios of ASASSN-20hx are somewhat soft, they are still harder than many other X-ray-luminous TDEs like ASASSN-14li (Holoien et al. 2016a) and ASASSN-19dj (Hinkle et al. 2021b).

4.2. AGN-like Features of ASASSN-20hx

The first characteristic of ASASSN-20hx that suggests a potential AGN origin is the archival Swift-XRT X-ray detection. At a luminosity of $(2.2 \pm 1.4) \times 10^{41}\,\mathrm{erg\,s^{-1}}$, with little star formation in the host, the X-rays are likely to originate from an LLAGN (Tozzi et al. 2006; Marchesi et al. 2016; Liu et al. 2017; Ricci et al. 2017). Given the host stellar mass, this X-ray luminosity is roughly two orders of magnitude higher than expected from low-mass X-ray binaries (Gilfanov 2004).

Indeed, the X-ray properties of ASASSN-20hx are generally consistent with an AGN. The power-law spectrum with a photon index of $\Gamma \sim 2.3$ is typical of an unobscured AGN. The hardness ratios are soft, but within the range seen for other AGNs (Auchettl et al. 2018). Additionally, the Eddington ratios measured from the X-ray emission and the peak UV/optical luminosity are much more consistent with low-luminosity AGNs (e.g., Ricci et al. 2017) than a typical TDE (e.g., Mockler et al. 2019).

While the SED of ASASSN-20hx is TDE-like in terms of its blackbody nature and persistent hot temperature, the temporal evolution of ASASSN-20hx in terms of blackbody properties is similar to other ANTs that have been argued to be of AGN origin in the literature. In Figure 15, the luminosity decline of ASASSN-20hx is similar to ASASSN-18el (Trakhtenbrot et al. 2019a) and ASASSN-17cv (AT2017bgt; Trakhtenbrot et al. 2019b). This is further supported by the narrow range in the ΔL_{40} decline rates seen in the ANTs in Figure 16. Similar to the other AGN-related transients, ASASSN-20hx has a relatively large effective blackbody radius. In fact, whereas most TDEs have shrinking blackbody radii over time (Hinkle et al. 2020a; van Velzen et al. 2021), ASASSN-20hx and the other ANTs have roughly constant effective radii for over a year. All of the nuclear transients shown in Figure 15 are hot, but ASASSN-20hx and the other non-TDE transients have among the coolest blackbody temperatures. This is perhaps due to the more massive black holes where these transients tend to occur (e.g., Shakura & Sunyaev 1973).

Save for the archival X-ray detection, the host galaxy of ASASSN-20hx does not have many clear signs of AGN activity. Figure 1 shows the WISE color–color selection of Assef et al. (2013) along with well-studied ANTs and TDEs. Most ANTs and TDEs lie far from the shaded gray region that indicates AGN selection, but the host galaxy of ASASSN-20hx has the bluest $W1 - W2$ color. The host galaxy of ASASSN-20hx is classified as an AGN in the [N II]/Hα diagram, its classification is ambiguous in the [S II]/Hα diagram, and it would not be classified as an AGN in the WHAN diagram. This lack of consistent classification makes it unlikely that the host galaxy of ASASSN-20hx was a strong AGN.

The lack of H, He, N, O, and S optical and NIR emission lines is also difficult to reconcile with an AGN origin. In the spectra of ASASSN-20hx, these lines are all very weak or absent entirely. Normal AGN all have emission lines (e.g., Ho 2008) that typically increase in strength during a flare (e.g., Trakhtenbrot et al. 2019b; Frederick et al. 2019, 2020). Even if
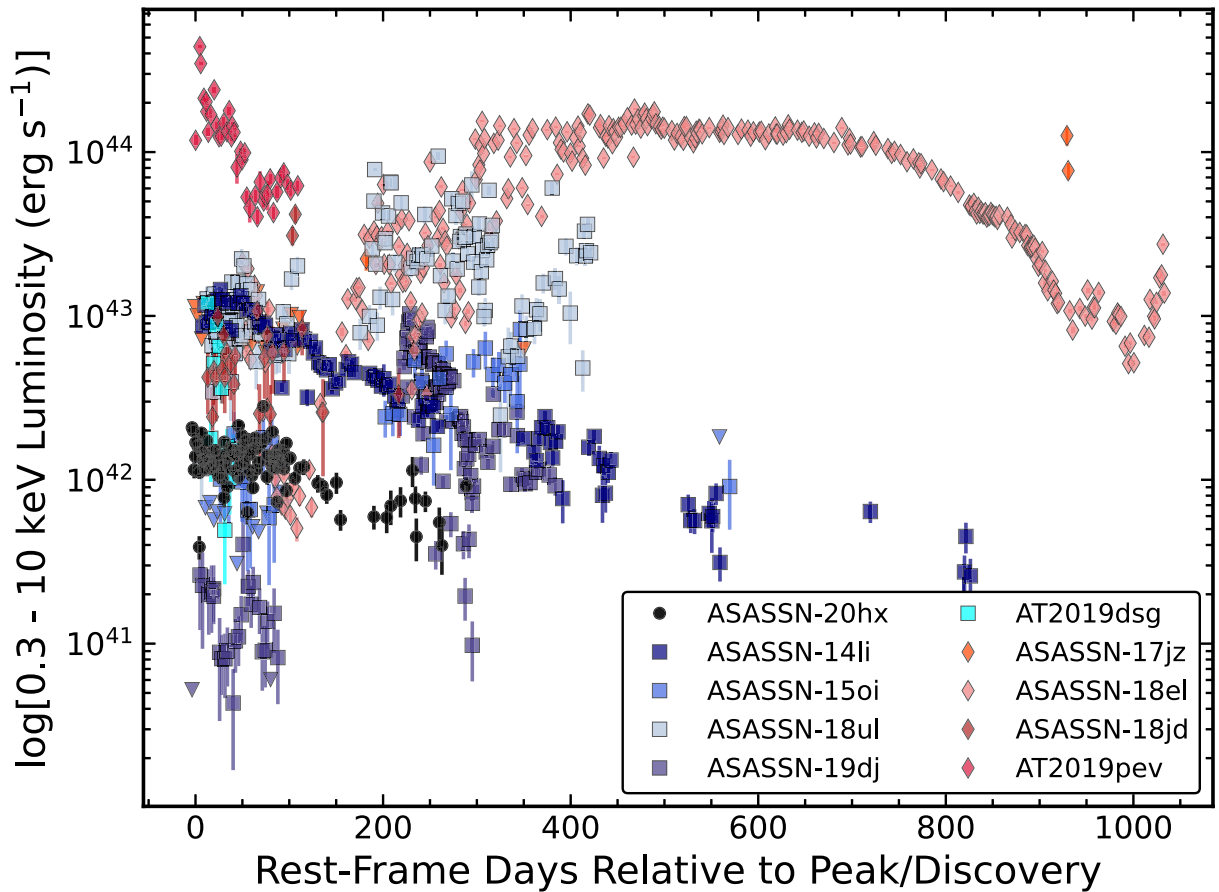
Figure 19. Evolution of the 0.3–10 keV X-ray luminosities for ASASSN-20hx (black squares) and a comparison sample of TDEs (blue squares) and ANTs (red diamonds). Time is in rest-frame days relative to the peak UV/optical luminosity for the objects discovered prior to peak (ASASSN-18ul, ASASSN-19dj, AT2019dsg, ASASSN-17jz, and AT2019pev) and relative to discovery for those that were not (ASASSN-18el, ASASSN-18jd, ASASSN-15oi, and ASASSN-14li).

we were to imagine a scenario where low-ionization lines were not produced during the ASASSN-20hx flare, we might expect the high level of UV and X-ray photons to produce the coronal lines often seen in AGNs (Lamperti et al. 2017). However, as shown in Figure 13, none of these commonly seen lines are present in the NIR spectra of ASASSN-20hx, further challenging a typical AGN picture.

One class of objects with AGN-like X-ray emission without corresponding optical AGN lines are the XBONGs (X-ray Bright Optically Normal Galaxies; Moran et al. 2002; Smith et al. 2014), although these typically do not lack emission lines entirely. If the lack of emission lines seen for ASASSN-20hx is simply the result of missing gas in the nucleus, continued follow-up over several years may reveal narrow lines at later times. Additionally, blazars show featureless continua with no emission lines, but here we would likely expect radio emission if the jet is not significantly self-absorbed.

4.3. Comparing TDE and AGN Scenarios

Using the framework of Frederick et al. (2020), we can compare the various characteristics of ASASSN-20hx and assign them to a more AGN-like or more TDE-like classification, with the results shown in Table 7. This classification method was developed for transients occurring in narrow-line Seyfert 1 galaxies, but the basic principles can be applied more broadly. First, the SMBH mass for ASASSN-20hx is below 10^8 $M_\odot$, and thus is consistent with a TDE. As there is no measured

hydrogen emission during the outburst, we cannot compute a line width to discriminate between typical TDE and AGN line widths. We do not observe Fe II emission from ASASSN-20hx, consistent with a TDE as opposed to an AGN. The UV/optical colors are roughly constant over time, which is consistent with a TDE, as is the UV luminosity of the event. The existence of a power-law-like X-ray emission at a relatively hard photon index is more consistent with an AGN than a TDE. As previously mentioned, the WISE colors of the host are inconsistent with a strong AGN, although these data are of the quiescent host emission. Finally, while the slow decrease in the luminosity of ASASSN-20hx over time with no significant rebrightenings is consistent with a TDE, the very long overall timescale for fading is more consistent with known transients in AGNs rather than typical TDEs.

In addition to the events studied in Frederick et al. (2020), there have been several claims in the literature of TDEs occurring in galaxies hosting an AGN. These include PS16dtm (Blanchard et al. 2017) and ASASSN-18el (Ricci et al. 2020). In these cases, the host galaxies were known AGNs and the transient emission and evolution were argued to be consistent with a TDE superimposed on top of the existing AGN variability. Such a scenario is possible for ASASSN-20hx and could help explain the existence of TDE-like UV/optical emission with AGN-like X-ray emission. Nonetheless, such a scenario is speculative and difficult to prove definitively. In addition, the optical and NIR spectra (detailed in Table 8) are still inconsistent with this picture, so such an explanation does

not allow us to neatly explain the full range of observed properties for ASASSN-20hx.

5. Summary

We have presented the discovery of the ANT ASASSN-20hx and detailed the multiwavelength photometric and spectroscopic follow-up data we have obtained on this event. The key properties of ASASSN-20hx are as follows:

1. The host galaxy of ASASSN-20hx did not host a strong AGN prior to the transient.
2. The rise in flux of ASASSN-20hx is well constrained by TESS photometry with a power-law slope of $\alpha = 1.05 \pm 0.06$, which is shallower than the $\alpha \sim 2$ previously seen in TDEs.
3. The UV/optical SED of ASASSN-20hx is well fit by a blackbody with a roughly constant temperature of $\sim$21,000 K and a peak luminosity of 3.2×10^{43} erg s^{-1}. The evolution of the blackbody properties is qualitatively consistent with previous TDEs and ANTs, but not typical AGNs.
4. The optical and NIR spectra of ASASSN-20hx are devoid of emission lines, which is problematic for either an AGN or a TDE explanation for this transient.
5. The host galaxy of ASASSN-20hx was detected as an X-ray source prior to the ASASSN-20hx flare. The X-ray emission associated with ASASSN-20hx is roughly an order of magnitude higher and well fit by a power law with $\Gamma \sim 2.3$–2.6, consistent with AGN-like emission.

Many of the observed properties of ASASSN-20hx can be reconciled through the TDE or AGN explanation, or in some cases both. However, the lack of emission lines proves difficult to explain in either case. Nonetheless as ASASSN-20hx continues to evolve and we continue to add more ANTs to our growing sample, we will be able to better understand the full range of behaviors occurring in galactic nuclei.

ORCID iDs

Jason T. Hinkle ◉ https://orcid.org/0000-0001-9668-2920
Thomas W.-S. Holoien ◉ https://orcid.org/0000-0001-9206-3460
Benjamin. J. Shappee ◉ https://orcid.org/0000-0003-4631-1149
Jack M. M. Neustadt ◉ https://orcid.org/0000-0001-7351-2531
Katie Auchettl ◉ https://orcid.org/0000-0002-4449-9152
Melissa Shahbandeh ◉ https://orcid.org/0000-0002-9301-5302

Matthias Kluge ⬤ https://orcid.org/0000-0002-9618-2552
Christopher S. Kochanek ⬤ https://orcid.org/0000-0001-6017-2961
Mark E. Huber ⬤ https://orcid.org/0000-0003-1059-9603
David Bersier ⬤ https://orcid.org/0000-0001-7485-3020
Christopher Ashall ⬤ https://orcid.org/0000-0002-5221-7557
Michael A. Tucker ⬤ https://orcid.org/0000-0002-2471-8442
Jonathan P. Williams ⬤ https://orcid.org/0000-0001-5058-695X
Aaron Do ⬤ https://orcid.org/0000-0003-3429-7845
Michael Fausnaugh ⬤ https://orcid.org/0000-0002-9113-7162
Daniel Gruen ⬤ https://orcid.org/0000-0003-3270-7644
Ulrich Hopp ⬤ https://orcid.org/0000-0003-1008-225X
Justin Myles ⬤ https://orcid.org/0000-0001-6145-5859
Christian Obermeier ⬤ https://orcid.org/0000-0002-3819-8855
Anna V. Payne ⬤ https://orcid.org/0000-0003-3490-3243
Todd A. Thompson ⬤ https://orcid.org/0000-0003-2377-9574

References

2MASS 2020, 2MASS All-Sky Atlas Image Service, IPAC, doi:10.26131/IRSA121
Adelman-McCarthy, J. K., Agüeros, M. A., Allam, S. S., et al. 2006, ApJS, 162, 38
Aguado, D. S., Ahumada, R., Almeida, A., et al. 2019, ApJS, 240, 23
Alard, C. 2000, A&AS, 144, 363
Alard, C., & Lupton, R. H. 1998a, ApJ, 503, 325
Alexander, K. D., van Velzen, S., Horesh, A., & Zauderer, B. A. 2020, SSRv, 216, 81
Antonucci, R. 1993, ARA&A, 31, 473
Arcavi, I., Gal-Yam, A., Sullivan, M., et al. 2014, ApJ, 793, 38
Arnaud, K. A. 1996, in ASP Conf. Ser. 101, Astronomical Data Analysis Software and Systems V, ed. G. H. Jacoby & J. Barnes (San Francisco, CA: ASP), 17
Assef, R. J., Kochanek, C. S., Brodwin, M., et al. 2010, ApJ, 713, 970
Assef, R. J., Stern, D., Kochanek, C. S., et al. 2013, ApJ, 772, 26
Atkinson, J. W., Collett, J. L., Marconi, A., et al. 2005, MNRAS, 359, 504
Auchettl, K., Guillochon, J., & Ramirez-Ruiz, E. 2017, ApJ, 838, 149
Auchettl, K., Ramirez-Ruiz, E., & Guillochon, J. 2018, ApJ, 852, 37
Baldwin, J. A., Phillips, M. M., & Terlevich, R. 1981, PASP, 93, 5
Barron, J. T., Stumm, C., Hogg, D. W., Lang, D., & Roweis, S. 2008, AJ, 135, 414
Batra, N. D., & Baldwin, J. A. 2014, MNRAS, 439, 771
Bellm, E. C., Kulkarni, S. R., Graham, M. J., et al. 2019, PASP, 131, 018002
Bentz, M. C., Walsh, J. L., Barth, A. J., et al. 2010, ApJ, 716, 993
Bertin, E., & Arnouts, S. 1996, A&AS, 117, 393
Bianchi, S., Guainazzi, M., Matt, G., et al. 2005, A&A, 442, 185
Blagorodnova, N., Gezari, S., Hung, T., et al. 2017, ApJ, 844, 46
Blagorodnova, N., Karambelkar, V., Adams, S. M., et al. 2020, MNRAS, 496, 5503
Blanchard, P. K., Nicholl, M., Berger, E., et al. 2017, ApJ, 843, 106
Bogdanov, S., Guillot, S., Ray, P. S., et al. 2019, ApJL, 887, L25
Boroson, T. A., & Green, R. F. 1992, ApJS, 80, 109
Bose, S., Dong, S., Pastorello, A., et al. 2018, ApJ, 853, 57
Breeveld, A. A., Curran, P. A., Hoversten, E. A., et al. 2010, MNRAS, 406, 1687
Brimacombe, J., Cacella, P., Marples, P., et al. 2020, ATel, 13891, 1
Brinchmann, J., Charlot, S., White, S. D. M., et al. 2004, MNRAS, 351, 1151
Brown, J. S., Holoien, T. W.-S., Auchettl, K., et al. 2017, MNRAS, 466, 4904
Brown, J. S., Kochanek, C. S., Holoien, T. W.-S., et al. 2018, MNRAS, 473, 1130
Brown, T. M., Baliber, N., Bianco, F. B., et al. 2013, PASP, 125, 1031
Bruzual, G., & Charlot, S. 2003, MNRAS, 344, 1000
Burrows, D. N., Hill, J. E., Nousek, J. A., et al. 2005, SSRv, 120, 165
Cannizzaro, G., Wevers, T., Jonker, P. G., et al. 2021, MNRAS, 504, 792
Cardelli, J. A., Clayton, G. C., & Mathis, J. S. 1988, ApJL, 329, L33
Cendes, Y., Alexander, K. D., Berger, E., et al. 2021, ApJ, 919, 127
Chambers, K. C., Magnier, E. A., Metcalfe, N., et al. 2016, arXiv:1612.05560
Chornock, R., Berger, E., Gezari, S., et al. 2014, ApJ, 780, 44
Cid Fernandes, R., Stasińska, G., Mateus, A., & Vale Asari, N. 2011, MNRAS, 413, 1687
Cutri, R. M., Wright, E. L., Conrow, T., et al. 2021, VizieR Online Data Catalog, II/328

D'Agostino, J. J., Kewley, L. J., Groves, B. A., et al. 2019, MNRAS, 487, 4153
Davies, R. L., Kewley, L. J., Ho, I. T., & Dopita, M. A. 2014, MNRAS, 444, 3961
de Vaucouleurs, G., de Vaucouleurs, A., Corwin, H. G. J., et al. 1991, Third Reference Catalogue of Bright Galaxies (New York: Springer)
Denney, K. D., Peterson, B. M., Dietrich, M., Vestergaard, M., & Bentz, M. C. 2009, ApJ, 692, 246
Denney, K. D., De Rosa, G., Croxall, K., et al. 2014, ApJ, 796, 134
Dong, S., Shappee, B. J., Prieto, J. L., et al. 2016, Sci, 351, 257
Drake, A. J., Djorgovski, S. G., Mahabal, A., et al. 2009, ApJ, 696, 870
Eisenstein, D. J., Weinberg, D. H., Agol, E., et al. 2011, AJ, 142, 72
Evans, C. R., & Kochanek, C. S. 1989, ApJL, 346, L13
Evans, P. A., Fridriksson, J. K., Gehrels, N., et al. 2012, ApJS, 203, 28
Fausnaugh, M. M., Vallely, P. J., Kochanek, C. S., et al. 2021, ApJ, 908, 51
Ford, H. C., Harms, R. J., Tsvetanov, Z. I., et al. 1994, ApJL, 435, L27
Frederick, S., Gezari, S., Graham, M. J., et al. 2019, ApJ, 883, 31
Frederick, S., Gezari, S., Graham, M. J., et al. 2020, ApJ, 920, 56
French, K. D., Arcavi, I., & Zabludoff, A. 2016, ApJL, 818, L21
Gafton, E., & Rosswog, S. 2019, MNRAS, 487, 4790
Gal-Yam, A. 2012, Sci, 337, 927
Gebhardt, K., Adams, J., Richstone, D., et al. 2011, ApJ, 729, 119
Gehrels, N., Chincarini, G., Giommi, P., et al. 2004, ApJ, 611, 1005
Gendreau, K. C., Arzoumanian, Z., & Okajima, T. 2012, Proc. SPIE, 8443, 844313
Gezari, S., Cenko, S. B., & Arcavi, I. 2017, ApJL, 851, L47
Gezari, S., Chornock, R., Rest, A., et al. 2012, Natur, 485, 217
Ghez, A. M., Salim, S., Hornstein, S. D., et al. 2005, ApJ, 620, 744
Gilfanov, M. 2004, MNRAS, 349, 146
Graham, M. J., Djorgovski, S. G., Drake, A. J., et al. 2017, MNRAS, 470, 4112
Gromadzki, M., Hamanowicz, A., Wyrzykowski, L., et al. 2019, A&A, 622, L2
Guillochon, J., Nicholl, M., Villar, V. A., et al. 2017, MOSFiT: Modular Open-Source Fitter for Transients, Astrophysics Source Code Library, ascl:1710.006
Guillochon, J., & Ramirez-Ruiz, E. 2015, ApJ, 809, 166
Haggard, D., Green, P. J., Anderson, S. F., et al. 2010, ApJ, 723, 1447
Henden, A. A., Levine, S., Terrell, D., & Welch, D. L. 2015, AAS Meeting Abstracts, 225, 336.16
HI4PI Collaboration, Ben Bekhti, N., Flöer, L., et al. 2016, A&A, 594, A116
Hill, J. M., Green, R. F., & Slagle, J. H. 2006, Proc. SPIE, 6267, 62670Y
Hinkle, J. T., Holoien, T. W. S., Shappee, B. J., & Auchettl, K. 2021a, ApJ, 910, 83
Hinkle, J. T., Holoien, T. W. S., Shappee, B. J., et al. 2020a, ApJL, 894, L10
Hinkle, J. T., Shappee, B. J., Holoien, T. W. S., et al. 2020b, ATel, 13893, 1
Hinkle, J. T., Holoien, T. W. S., Auchettl, K., et al. 2021b, MNRAS, 500, 1673
Ho, L. C. 2008, ARA&A, 46, 475
Holland, W. S., Bintley, D., Chapin, E. L., et al. 2013, MNRAS, 430, 2513
Holoien, T. W.-S., Brown, J. S., Auchettl, K., et al. 2018, MNRAS, 480, 5689
Holoien, T. W.-S., Prieto, J. L., Bersier, D., et al. 2014, MNRAS, 445, 3263
Holoien, T. W.-S., Kochanek, C. S., Prieto, J. L., et al. 2016a, MNRAS, 455, 2918
Holoien, T. W.-S., Kochanek, C. S., Prieto, J. L., et al. 2016b, MNRAS, 463, 3813
Holoien, T. W. S., Huber, M. E., Shappee, B. J., et al. 2019a, ApJ, 880, 120
Holoien, T. W.-S., Brown, J. S., Vallely, P. J., et al. 2019b, MNRAS, 484, 1899
Holoien, T. W. S., Vallely, P. J., Auchettl, K., et al. 2019c, ApJ, 883, 111
Holoien, T. W. S., Auchettl, K., Tucker, M. A., et al. 2020, ApJ, 898, 161
Holoien, T. W. S., Neustadt, J. M. M., Vallely, P. J., et al. 2021, arXiv:2109.07480
Hung, T., Foley, R. J., Ramirez-Ruiz, E., et al. 2020, ApJ, 903, 31
Hung, T., Foley, R. J., Veilleux, S., et al. 2021, ApJ, 917, 9
Irwin, J. A., Henriksen, R. N., Krause, M., et al. 2015, ApJ, 809, 172
Kara, E., Dai, L., Reynolds, C. S., & Kallman, T. 2018, MNRAS, 474, 3593
Kauffmann, G., & Heckman, T. M. 2009, MNRAS, 397, 135
Kauffmann, G., Heckman, T. M., Tremonti, C., et al. 2003, MNRAS, 346, 1055
Kochanek, C. S. 2016, MNRAS, 461, 371
Kochanek, C. S., Shappee, B. J., Stanek, K. Z., et al. 2017, PASP, 129, 104502
Kormendy, J., & Ho, L. C. 2013, ARA&A, 51, 511
Kriek, M., van Dokkum, P. G., Labbé, I., et al. 2009, ApJ, 700, 221
Lacerda, E. A. D., Sánchez, S. F., Cid Fernandes, R., et al. 2020, MNRAS, 492, 3073
Lacy, J. H., Townes, C. H., & Hollenbach, D. J. 1982, ApJ, 262, 120
Lamperti, I., Koss, M., Trakhtenbrot, B., et al. 2017, MNRAS, 467, 540

Landt, H., Bentz, M. C., Ward, M. J., et al. 2008, ApJS, 174, 282
Lang, D., Hogg, D. W., Mierle, K., Blanton, M., & Roweis, S. 2010, AJ, 139, 1782
Lantz, B., Aldering, G., Antilogus, P., et al. 2004, Proc. SPIE, 5249, 146
Leloudas, G., Fraser, M., Stone, N. C., et al. 2016, NatAs, 1, 0002
Leloudas, G., Dai, L., Arcavi, I., et al. 2019, ApJ, 887, 218
Leonard, D. C., & Filippenko, A. V. 2001, PASP, 113, 920
Lin, D. 2020, ATel, 13895, 1
Liu, T., Tozzi, P., Wang, J.-X., et al. 2017, ApJS, 232, 8
Lodato, G., & Rossi, E. M. 2011, MNRAS, 410, 359
Lunnan, R., Yan, L., Perley, D. A., et al. 2020, ApJ, 901, 61
Lupton, R. 2005, http://www.sdss.org/dr5/algorithms/sdssUBVRITransform.html
MacLeod, C. L., Ivezić, Ž., Sesar, B., et al. 2012, ApJ, 753, 106
MacLeod, C. L., Ross, N. P., Lawrence, A., et al. 2016, MNRAS, 457, 389
Magorrian, J., Tremaine, S., Richstone, D., et al. 1998, AJ, 115, 2285
Mainzer, A., Bauer, J., Grav, T., et al. 2011, ApJ, 731, 53
Malyali, A., Rau, A., Merloni, A., et al. 2021, A&A, 647, A9
Marchesi, S., Lanzuisi, G., Civano, F., et al. 2016, ApJ, 830, 100
Martin, D. C., Fanson, J., Schiminovich, D., et al. 2005, ApJL, 619, L1
McConnell, N. J., & Ma, C.-P. 2013, ApJ, 764, 184
Mendel, J. T., Simard, L., Palmer, M., Ellison, S. L., & Patton, D. R. 2014, ApJS, 210, 3
Merloni, A., Heinz, S., & di Matteo, T. 2003, MNRAS, 345, 1057
Million, C., Fleming, S. W., Shiao, B., et al. 2016, ApJ, 833, 292
Mockler, B., Guillochon, J., & Ramirez-Ruiz, E. 2019, ApJ, 872, 151
Moran, E. C., Filippenko, A. V., & Chornock, R. 2002, ApJL, 579, L71
Moretti, A., Campana, S., Tagliaferri, G., et al. 2004, Proc. SPIE, 5165, 232
Mummery, A. 2021, arXiv:2104.06212
Mummery, A., & Balbus, S. A. 2021, MNRAS, 504, 4730
Mushotzky, R. F., Done, C., & Pounds, K. A. 1993, ARA&A, 31, 717
NEOWISE 2020, NEOWISE-R Single Exposure (L1b) Source Table, IPAC, doi: 10.26131/IRSA144
Neustadt, J. M. M., Holoien, T. W. S., Kochanek, C. S., et al. 2020, MNRAS, 494, 2538
Nicholl, M., Wevers, T., Oates, S. R., et al. 2020, MNRAS, 499, 482
Oke, J. B., Cohen, J. G., Carr, M., et al. 1995, PASP, 107, 375
Paggi, A., Milisavljevic, D., Masetti, N., et al. 2014, AJ, 147, 112
Pasham, D., & Gendreau, K. 2020, ATel, 14248, 1
Pasham, D., Gendreau, K., Arzoumanian, Z., et al. 2020a, ATel, 14036, 1
Pasham, D., Gendreau, K., Remillard, R., et al. 2020b, ATel, 13864, 1
Payne, A. V., Shappee, B. J., Hinkle, J. T., et al. 2022, ApJ, 926, 142
Payne, A. V., Shappee, B. J., Hinkle, J. T., et al. 2021, ApJ, 910, 125
Perley, D. A. 2019, PASP, 131, 084503
Peterson, B. M., Ferrarese, L., Gilbert, K. M., et al. 2004, ApJ, 613, 682
Phinney, E. S. 1989, Natur, 340, 595
Piascik, A. S., Steele, I. A., Bates, S. D., et al. 2014, Proc. SPIE, 9147, 91478H
Pogge, R. W., Atwood, B., Brewer, D. F., et al. 2010, Proc. SPIE, 7735, 77350A
Poole, T. S., Breeveld, A. A., Page, M. J., et al. 2008, MNRAS, 383, 627
Poutanen, J., & Svensson, R. 1996, ApJ, 470, 249
Rayner, J. T., Toomey, D. W., Onaka, P. M., et al. 2003, PASP, 115, 362
Rees, M. J. 1988, Natur, 333, 523
Reguitti, A., Pumo, M. L., Mazzali, P. A., et al. 2021, MNRAS, 501, 1059
Reynolds, C. S. 1997, MNRAS, 286, 513
Reynolds, C. S. 2014, SSRv, 183, 277
Reynolds, C. S. 2019, NatAs, 3, 41

Ricci, C., Trakhtenbrot, B., Koss, M. J., et al. 2017, ApJS, 233, 17
Ricci, C., Kara, E., Loewenstein, M., et al. 2020, ApJL, 898, L1
Ricci, C., Loewenstein, M., Kara, E., et al. 2021, ApJS, 255, 7
Ricker, G. R., Winn, J. N., Vanderspek, R., et al. 2015, JATIS, 1, 014003
Rodrigo, C., Solano, E., & Bayo, A. 2012, SVO Filter Profile Service Version 1.0, IVOA Working Draft 15 October 2012, doi: 10.5479/ADS/bib/2012ivoa.rept.1015R
Roming, P. W. A., Kennedy, T. E., Mason, K. O., et al. 2005, SSRv, 120, 95
Roth, N., & Kasen, D. 2018, ApJ, 855, 54
Ryu, T., Krolik, J., Piran, T., & Noble, S. C. 2020, ApJ, 904, 98
Salpeter, E. E. 1955, ApJ, 121, 161
Sanders, D. B., Soifer, B. T., Elias, J. H., et al. 1988, ApJ, 325, 74
Sanders, N. E., Soderberg, A. M., Gezari, S., et al. 2015, ApJ, 799, 208
Saulder, C., van Kampen, E., Chilingarian, I. V., Mieske, S., & Zeilinger, W. W. 2016, A&A, 596, A14
Schlafly, E. F., & Finkbeiner, D. P. 2011, ApJ, 737, 103
Shakura, N. I., & Sunyaev, R. A. 1973, A&A, 500, 33
Shappee, B. J., Prieto, J. L., Grupe, D., et al. 2014, ApJ, 788, 48
Shi, Y., Rieke, G. H., Smith, P., et al. 2010, ApJ, 714, 115
Skrutskie, M. F., Cutri, R. M., Stiening, R., et al. 2006, AJ, 131, 1163
Smith, K. L., Koss, M., & Mushotzky, R. F. 2014, ApJ, 794, 112
Steele, I. A., Smith, R. J., Rees, P. C., et al. 2004, Proc. SPIE, 5489, 679
Taddia, F., Stritzinger, M. D., Bersten, M., et al. 2018, A&A, 609, A136
Tonry, J. L., Denneau, L., Heinze, A. N., et al. 2018, PASP, 130, 064505
Tozzi, P., Gilli, R., Mainieri, V., et al. 2006, A&A, 451, 457
Trakhtenbrot, B., Arcavi, I., MacLeod, C. L., et al. 2019a, ApJ, 883, 94
Trakhtenbrot, B., Arcavi, I., Ricci, C., et al. 2019b, NatAs, 3, 242
Tucker, M. A., Shappee, B. J., Vallely, P. J., et al. 2020, MNRAS, 493, 1044
Tucker, M. A., Shappee, B. J., Hinkle, J. T., et al. 2021, MNRAS, 506, 6014
Ulmer, A. 1999, ApJ, 514, 180
Vallely, P. J., Kochanek, C. S., Stanek, K. Z., Fausnaugh, M., & Shappee, B. J. 2021, MNRAS, 500, 5639
Vallely, P. J., Fausnaugh, M., Jha, S. W., et al. 2019, MNRAS, 487, 2372
van Velzen, S. 2018, ApJ, 852, 72
van Velzen, S., Gezari, S., Hung, T., et al. 2019, ATel, 12568, 1
van Velzen, S., Farrar, G. R., Gezari, S., et al. 2011, ApJ, 741, 73
van Velzen, S., Gezari, S., Hammerstein, E., et al. 2021, ApJ, 908, 4
Vanden Berk, D. E., Richards, G. T., Bauer, A., et al. 2001, AJ, 122, 549
Vanderspek, R., Doty, J., Fausnaugh, M., et al. 2018, TESS Instrument Handbook, Tech. rep., Kavli Institute for Astrophysics and Space Science, Massachusetts Institute of Technology
Veilleux, S., & Osterbrock, D. E. 1987, ApJS, 63, 295
Wevers, T. 2020, MNRAS, 497, L1
Wevers, T., van Velzen, S., Jonker, P. G., et al. 2017, MNRAS, 471, 1694
Wevers, T., Pasham, D. R., van Velzen, S., et al. 2019a, MNRAS, 488, 4816
Wevers, T., Stone, N. C., van Velzen, S., et al. 2019b, MNRAS, 487, 4136
Wevers, T., Pasham, D. R., van Velzen, S., et al. 2021, ApJ, 912, 151
Wright, E. L., Eisenhardt, P. R. M., Mainzer, A. K., et al. 2010, AJ, 140, 1868
Wright, E. L., Eisenhardt, P. R. M., Mainzer, A. K., et al. 2019, AllWISE Source Catalog, IPAC, doi:10.26131/IRSA1
Yang, Q., Wu, X.-B., Fan, X., et al. 2018, ApJ, 862, 109
York, D. G., Adelman, J., Anderson, J. E., Jr., et al. 2000, AJ, 120, 1579
Yuan, Q., Wang, Q. D., Lei, W.-H., Gao, H., & Zhang, B. 2016, MNRAS, 461, 3375
Zhang, S., Baganoff, F. K., Ponti, G., et al. 2017, ApJ, 843, 96